Solid State NMR Studies of Materials for Energy Technology

by

Chandana K. Nambukara Kodiweera Arachchilage

A dissertation submitted to the Graduate Faculty in Physics in partial fulfillment of the requirements for the degree of Doctor of Philosophy, The City University of New York

2010

This manuscript has been read and accepted for the Graduate Faculty in Physics in satisfaction of the dissertation requirement for the degree of Doctor of Philosophy.

Steve Greenbaum

Date

Chair of Examining Committee

Steve Greenbaum

Date

Executive Officer

Frank Owens

Sophia Suarez

Ying-Chih Chen

Yuhang Ren

Supervisory Committee

THE CITY UNIVERSITY OF NEW YORK

Abstract

SOLID STATE NMR STUDIES OF MATERIALS FOR ENERGY TECHNOLOGY

by

Chandana K. Nambukara Kodiweera Arachchilage

Adviser: Professor Steve Greenbaum

Presented in this dissertation are NMR investigations of the dynamical and structural properties of materials for energy conversion and storage devices. ^1H and ^2H NMR was used to study water and methanol transportation in sulfonated poly(arylene ether ketone) based membranes for direct methanol fuel cells (DMFC). These results are presented in chapter 3. The amount of liquid in the membrane and ion exchange capacity (IEC) are two main factors that govern the dynamics in these membranes. Water and methanol diffusion coefficients also are comparable. Chapters 4 and 5 are concerned with ^{31}P and ^1H NMR in phosphoric acid doped PBI membranes (para-PBI and 2OH-PBI) as well as PBI membranes containing ionic liquids (H_3PO_4/$PMIH_2PO_4$/PBI). These membranes are designed for higher-temperature fuel cell operation. In general, stronger short and long range interactions were observed in the 2OH-PBI matrix, yielding reduced proton transport compared to that of para-PBI. In the case of H_3PO_4/$PMIH_2PO_4$/PBI, both conductivity and diffusion are higher for the sample with molar ratio 2/4/1. Finally, chapter 6 is devoted to the ^{31}P NMR MAS study of phosphorus-containing structural groups on the surfaces of micro/mesoporous activated carbons. Two spectral features were observed and the narrow feature identifies surface phosphates while the broad component identifies heterogeneous subsurface phosphorus environments including phosphate and more complex structure multiple P-C, P-N and P=N bonds.

To my Parents, Devasiri Kodiweera and Hemalatha Kodiweera.

Acknowledgements

I would like to thank: my mentor, Prof. Steven Greenbaum, for all his support , guidance and advice; Prof. Phil Stallworth for introducing me to experimental NMR; Prof. J.R.P. Jayakody for helping me to gain admission to CUNY Ph.D program; Dr. Sunil Dehipawala and his wife, Nandani Dehipawala, for being with us and for their friendship which helped prevent our isolation in the New York City; Dr. Gabriel Goenaga for being my brother-like friend; Dr. Amish Khalfan for being a good friend; Dr. Nicole Leifer, Dr. Shantha Amarasinghe, Dr. Arun Rajam, Guy Okoko, Jaime Farrington and Sohan De Silva for being friends and sharing their knowledge with me.

I should mention my beloved son, Doyen Kodiweera, and wife, Lankika Kodiweera. Their love made my graduate life joyful.

Table of Contents

Chapter 1: Introduction

Chapter 2: Solid state NMR

2.3. Fundamental interpretation for condensed matter

2.6. NMR pulse sequences

Chapter 3: ^{1}H and ^{2}H NMR PFG diffusion studies of POLYFUEL Inc. membranes

3.2. Experimental

Chapter 4: PBI – Phosphoric acid membranes

4.3. Results and discussion

Chapter 5: PBI - Ionic liquid membranes

Chapter 6: Activated carbon study

List of Tables

Chapter 3

Chapter 4

Chapter 6

List of Figures

Chapter 1

Chapter 2

Chapter 3

Chapter 4

Chapter 5

Chapter 6

Chapter 1

Introduction

This thesis contains descriptions of fundamental experimental work conducted on various state-of-the-art polymeric, gel, amorphous and polycrystalline substances. The goal of this work was to address certain structural and dynamical aspects of materials useful for the development of alternative energy devices. The experimental methods employed in these studies are techniques developed for solid-state nuclear magnetic resonance (NMR), as these methods can be universally applied to a wide variety of systems. The following thesis gives an overview of the research thrust and includes an introduction, theoretical description, and project specifics. To provide context, the **Introduction** section begins with a description of the energy devices, along with the relevant physico-chemical issues concerning the materials components**.** An introduction of the use of solid-state NMR as an experimental method is given at the end of the chapter.

1.1 The Devices

Proton Exchange Membrane and Direct Methanol Fuel Cells

Technological advancement for generation and distribution of electrical power as well as for enhanced performance in current technologies is extremely important in order to address our future energy needs. Among the existing technologies, proton exchange membrane (PEM) fuel cells are in the forefront. PEM fuel cells can conceivably have wide application in the perceived hydrogen-economy as there are a number of benefits that they offer: 1) the utilization of lower-cost fuels and technologies (i.e. hydrogen from natural gas and methanol), 2) potential incorporation into typical consumer devices (i.e. from laptop computers to automobiles), 3) lower environmental impact when compared to conventional coal and petroleum burning technologies. In addition, since PEM cells operate at relatively low temperatures (around 80°C), the overall device efficiency is higher, producing around 40-50 % of the maximum theoretical power [1]. PEM fuel cells can also vary their output quickly in order to adjust with power demand.

PEM fuel cells, being electrochemical devices, have 3 essential parts, as shown in fig 1.1: the anode, the cathode, and the electrolyte. The basic operation commences as fuel (hydrogen gas) is pumped into the anode side. A catalyst at the anode breaks the hydrogen down into H^+ (proton) and e^-.

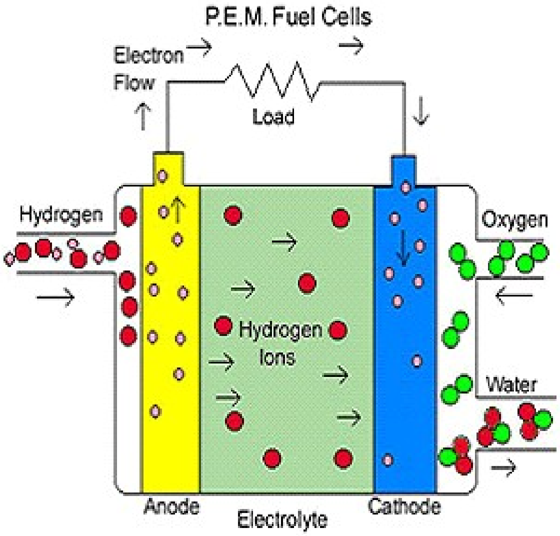

Figure 1.1 Operation of a PEM Fuel Cell

At this point the proton and electron go their separate ways. The proton migrates from the anode to cathode via the electrolyte, while the electron is free to power the external circuit (load). These particles then recombine at the cathode and react with oxygen (from air) to produce water as waste. A concise picture shows that PEM fuel cells generate electricity through the following chemical reaction:

Anode: $2H_2 \rightarrow 4H^+ + 4e^-$

Cathode: $O_2 + 4H^+ + 4e^- \rightarrow 2H_2O$

Overall: $2H_2 + O_2 \rightarrow 2H_2O$ + energy

A single anode/electrolyte/cathode unit is called a membrane electrode assembly (MEA). The MEA is sandwiched between two conductive field-flow plates which function to conduct electrons out of the assembly and channel hydrogen and oxygen (air) to the electrodes. Each cell produces around 0.7 volt; therefore, in order to generate higher voltages MEAs are combined in series, a.k.a. fuel cell stack.

The use of pure hydrogen as a fuel is currently not a universal practice for commercial PEM devices [2]. A substantial amount of PEM fuel cell development is geared towards the production of electricity from simple hydrocarbon fuels, i.e. via CH_3OH. As shown in figure 1.2, direct methanol fuel cell (DMFC) operation commences at the anode where methanol / water is catalyzed to produce the wanted current ($6e^-$) and CO_2 is produced as waste. For every CH_3OH molecule, the electrolyte membrane allows for protonic transport ($6H^+$) through to the cathode. Again, at the cathode water is produced as waste by recombination with oxygen from the air.

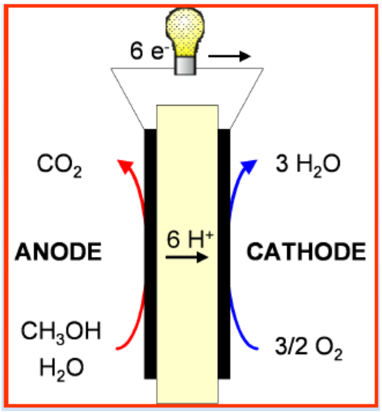

Figure 1.2 Fundamental DMFC Operation

One of the central topics of investigation, as described in this thesis, is the fundamental nature of the polymer electrolyte membrane. As for the DMFC, any unreacted methanol can diffuse through the polymer electrolyte membrane, creating a mixed potential at the cathode and affecting the overall performance of the cell [3]. This is called the methanol crossover and it is necessary to understand the nature of the methanol transport processes within the membrane to optimize the fuel cell performance.

The operation of the direct methanol fuel cell relies on the physico-chemical properties of the polymer electrolyte membrane. The main challenge for fuel cell membrane development is to enhance proton conductivity while reducing methanol crossover. Perfluorinted ionomers (PFI) such as Nafion (DuPont), Aciplex (Asahi Chemicals), Flemion (Asahi Glass) and Dow (Dow Chemicals) are widely used in DMFC. But, the limiting issues with these membranes are the high methanol crossover, incapability of maintaining water above 100 ^{0}C and their high cost [4]. In order to address these concerns, new membranes have been developed by POLYFUEL Inc. These special membranes are related to the sulfonated poly(arylene ether ketone)

(SPAEK) family of polymers. The typical monomeric unit of the polymer is shown in figure 1.3.

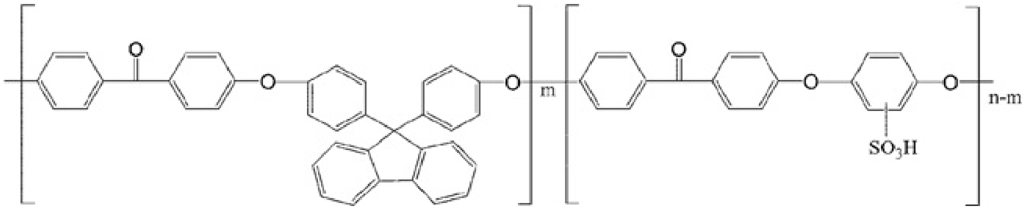

Figure 1.3: sulfonated poly(arylene ether ketone) (SPAEK) [14].

High mechanical strength, high thermal stability, low cost, moderate proton conductivity and low methanol crossover are the characteristics of the SPAEK. Poly (arylene ether ketone) (PAEK) is sulfonated to obtain SPAEK. As PAEK is hydrophobic, it does not conduct protons and therefore it has to transform into an electrolyte by sulfonation using sulfuric acid. Sulfonation replaces one of the hydrogen atom on aromatic rings with a sulfonic acid group (-SO_3H) [5]. This sulfonic acid group makes the SPAEK highly hydrophilic. The level of the degree of sulfonation (DS) determines the solubility of SPAEK. Sulfonic group is also responsible for the methanol crossover. Increasing Ion Exchange Capacity (IEC) means increasing the density of sulfonic groups. By increasing IEC, proton transport can be increased; methanol crossover also increases at the same time [6]. POLYFUEL Inc. membranes have been developed with different IECs. NMR PFG diffusion along with linewidth and relaxation studies on these membranes is reported in chapter 3.

Another PEM project reported in this thesis concerns membranes based on polybenzimidazole (PBI). These membranes find their application in PEM fuel cells that operate at higher temperatures (T >100 ^{0}C). Such high temperature operation avoids the necessity of using a highly sensitive and expensive catalyst on the electrodes, such as the metallic Pt/Ru blend currently used in PEM fuel cells [2]. High-temperature operation also reduces the formation and accumulation of CO, which substantially reduces the efficacy of the catalyst (electrode poisoning). The temperature issue arises since PEM fuel cell function is constrained by the properties of the electrolyte membrane, i.e. the ability to maintain the desired water content for successful proton transport. In the case of perflourosulfonic acid-based membranes, such as Nafion, operation at elevated temperatures is not feasible for this reason as previously mentioned. PBI-based membranes avoid the hydration issue (and therefore can operate at higher temperatures) because proton transport is mediated by a non-aqueous mechanism. Phosphoric acid based PBI membranes have shown stability at higher temperatures as both phosphoric acid and PBI have high thermal, chemical and mechanical stability, even at 180 ^{0}C. As described in chapters 4 and 5, research projects were carried out to investigate phosphoric acid based PBI membranes. Two sets of polymer samples were studied, as shown in figure 1.4 by the Rensselaer Polytechnic Institute (RPI) group and in figure 1.5 by the Rutgers University group.

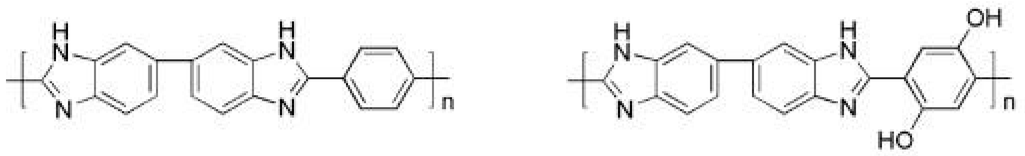

a b

Figure 1.4: a) para-PBI b). 2OH-PBI, samples were doped with different amount of phosphoric acid (30%, 50% and 70%)

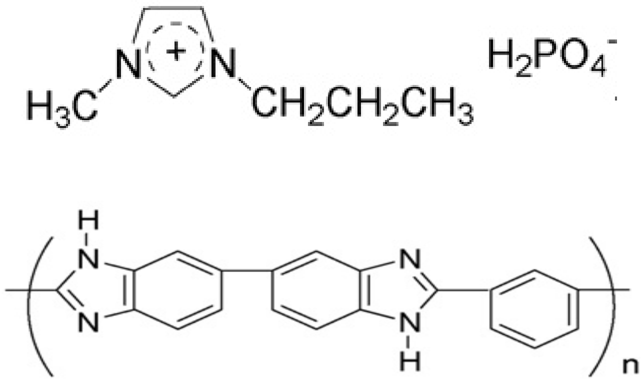

Figure 1.5: Ionic liquid based composite membrane: 1- methyl 3-propyl imidazolium dihydrogen phosphate ($PMIH_2PO_4$) *top*, polybenzimidazole (PBI) *bottom.* Three different composite membranes were cast with various molar ratios (4:2:1, 3:3:1 and 2:4:1 of $H_3PO_4/PMIH_2PO_4/PBI$).

NMR diffusion, relaxations and spectral analysis were carried on membranes (figure 1.4) produced by Rutgers university group and presented in chapter 4. The composite membrane shown in figure 1.5 was investigated using NMR techniques and presented in chapter 5. The latter demonstrates the feasibility of the concept of [acid/ionic liquid/polymer] composite gel-type proton conducting membranes that can serve as practical membranes for operation of PEM fuel cells at 150 °C while previous one investigates the dynamics by varying acid content in the PBI.

Supercapacitors

Supercapacitors (also known as ultracapacitors, electrochemical capacitors, or double layer capacitors) are electrochemical devices that have the ability to store and release charge and deliver high power densities over short periods of time. In these devices, no chemical processes are involved and therefore recyclability is higher, typically 10^5- 10^6 times. Their ability to store electrical energy efficiently and release electrical energy very quickly make them ideally suited for applications where short time backup power and peak power needs are critical. The basic picture is given in fig. 1.6.

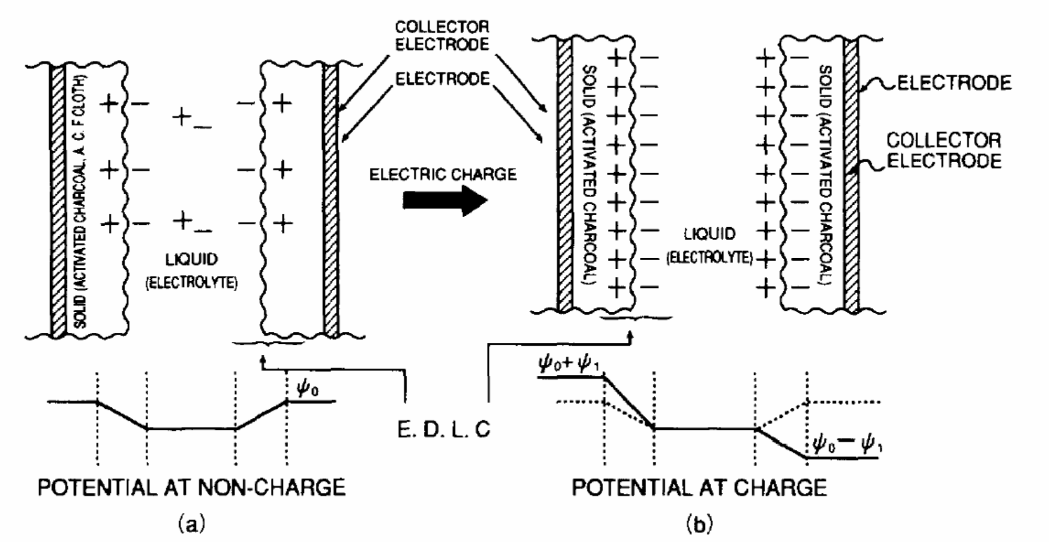

Figure 1.6: a) uncharged supercapacitor b) Charged supercapacitor, two double layers have formed [15].

Like conventional capacitors, supercapacitors also have two electrodes with a large surface area necessary for the accommodation and separation of charges. The capacitance can be as high as ~100 $\mu F/cm^2$ [7-8]. The electrodes are made of carbon based materials typically with specific surface area of about 1000 m^2/g [9]. In contrast to conventional capacitors, supercapacitors make use of electrolytes instead of a dielectric medium and therefore have the ability to store electrochemical energy at the interface between electrodes and the electrolyte. Both liquid and solid electrolytes can be used in supercapacitors. However, taking charging times into account, fast ion conductivity is a requirement. As well, the electrolyte should not transport electrons. In the electrolyte, mobile charge carriers with a positive charge can accumulate near a negatively charged electrode and vice versa (see Fig. 1.6 b). In this way a space charge region is developed in the electrolyte near the interface with the electrode and a large electrochemical capacitance is obtained. As shown in figure 1.6b, two double layers have formed after charging. The maximum voltage that can be applied to the electrodes is limited by the dissociation potential of the electrolyte [7]. Commonly used materials for electrolytes are, amongst others, ion-conducting polymers, also known as ionomers [10]. However, the ion conduction is often poor, which can be solved by using aqueous solutions of KOH or H_2SO_4 [11, 12] at the risk of obtaining leakage in these liquid electrolytes.

In addition to the capacitance that arises from the separation of charge in the double-layer, a contribution to capacitance can be made from reactions that can occur on the surface of the electrode. The charge required to facilitate these reactions is dependent on the potential, resulting in a Faradaic ‘pseudocapacitance’.

The high energy content of supercapacitors originates from the extremely high specific surface area and short distances between electrodes. Activated carbon materials are popular as supercapacitor electrodes owing to their high surface area. The porous structure and particularly the optimal pore size are the most influential factors determining the capacitive performance. Apart from the porous structure, activated carbons can be designed for a complex surface chemistry with the desired electrochemical energy storage for a given application. In chapter 6 is reported an NMR MAS investigation of granulated carbon activated on the surface with various phosphorus based oxides and nitrogen containing compounds. Figure 1.7 provides a picture of activated carbon.

Figure 1.7: Activated Carbon, the particulate nature and large porosity gives a very large surface area available for adsorption and chemical reactions [16].

Six activated carbon samples of wood origin were studied, sample code: BAX-1500 (Mead Westvaco). The carbons were either modified by urea (U) or melamine (M) and/or were pre-oxidized (O): BAX, BAX-O, BAX-U, BAX-UO, BAX-M, BAX-MO.

Solid-state NMR studies of activated carbons were performed in order to study the link of electrochemical performance with the physico-chemical nature of the carbon surface and results are presented in chapter 6.

1.2 **Solid-State NMR**

Nuclear magnetic resonance (NMR) continues to be a powerful spectroscopic method for structural and dynamical studies of condensed matter systems. NMR has particular value in applications where other techniques fail or have limited viability, such as in the study of amorphous solids (polymers, glasses, gels, heterogeneous materials, etc) and in studies where sample integrity must be maintained (biological applications). An important feature of NMR is that information gathered from the technique is nucleus specific, and nuclei serve as 'probes' of structure and dynamics on an atomic and molecular scale. Much contemporary research in the field is geared towards extending NMR to probe structure on larger scales via imaging techniques. Since nuclei have intrinsic angular momentum or spin, NMR is also spin dependent and useful only in cases where spin $I \geq 1/2$, $(I \neq 0)$. For instance, this means that NMR cannot be used to study the two highly abundant nuclei ^{12}C and ^{16}O. However, carbon and oxygen environments can be probed by ^{13}C and ^{17}O NMR. In some cases isotopically enriched materials must be prepared. Another important feature of NMR is that certain aspects of the structure and/or dynamics can be monitored more or less by manipulation of the nuclear spin system through the application of rf (radio frequency) pulses. The use of *pulse sequences* to carry out experiments is now the universally accepted method. In this regard alone, NMR spectroscopy has become one of the most important analytical techniques for materials investigation.

The signal re-radiated from the sample in the NMR experiment as a result of the initial excitation pulse is in the form of an oscillating magnetization vector. This magnetization induces a current in a nearby pick-up coil, creating an oscillating electrical signal. This signal, called the free induction decay, or FID, is essentially a sum of all of the spin signals. In order to extract information, the FID must be Fourier transformed (see figure 1.8).

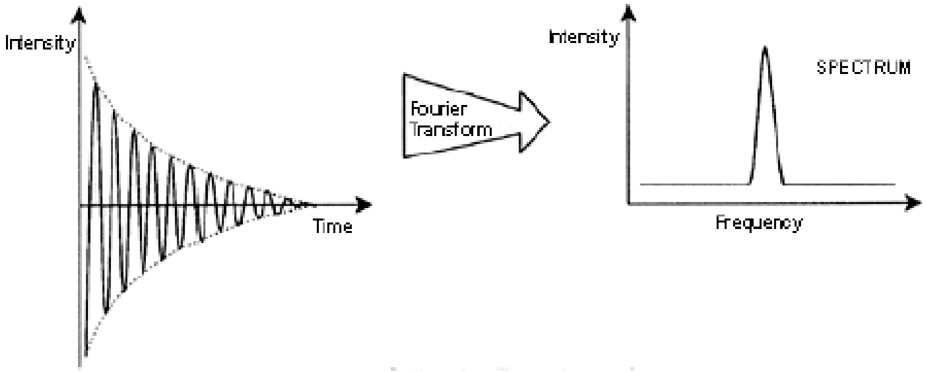

Figure 1.8: An example of a free induction decay (fid) signal, and its associated Fourier transform [17].

Another important technique that has been developed for the study of solid state systems is magic-angle spinning (MAS). The practical application of MAS reduces the effect of large nucleus-environment interactions that are typically observed in the resonances of solids. Theoretical and experimental details of pertaining to MAS lineshapes can be found in the chapter 2.

A number of NMR techniques have been developed for the study of dynamics (motion and relaxation). For example, in a solid electrolyte (i.e. proton exchange membrane as discussed later in this thesis), ionic conductivity can typically be measured by alternating current (AC) impedance methods. From such studies, only overall total charge transport can be gauged as it is often difficult to measure independently each contribution to the ionic conductivity. However due to its nuclear specificity, NMR can in principle study the motions of the various charge carriers independently.

Linewidth and relaxation measurements yield information about local motions within the system (polymer, crystal, liquid, gas, etc.). However, it can be difficult to extract direct information about translational motions from spectra and relaxation times alone. In simple isotropic systems D is shown to be related to the correlation time, τ_c, via $D = \frac{r^2}{6\tau_c}$, where r is the mean square jump distance of the diffusing nucleus [13]. In this picture the assumption is made that the relaxation process is directly related to the translational motion. But the connection between diffusion and relaxation is more complex in general. Fortunately, NMR techniques have been developed to directly monitor the translational motion of nuclear spins. Presented in this thesis are the application of pulsed-field-gradient NMR techniques and the measurement of the self diffusion coefficient, D. NMR diffusion theory and measurements are elaborated upon in chapters 2, 3, 4 and 5.

References

[1]. Rayment, C.; Sherwin, S.; “ Introduction to Fuel Cell Technology” *University of Notre Dame*, (2003).

[2]. Thomas, S.; Zalbowitz, M.; “ Fuel Cells – green power”, *Los Alamos National Laboratory, New Mexico*.

[3]. Scott, K.; Taama, W.M.; Argyropoulos, P.; Sundmacher, K.; “The impact of mass transport and methanol crossover on the direct methanol fuel cell” *J. Power Sources* 83 (1999) 204.

[4]. Jiang, R.; Kunz, H.R.; Fenton, J.M.; “Sulfonated Poly (Ether Ether Ketone) based membranes for direct methanol fuel cells (DMFC) applications” *the Electrochemical Co Inc*, Abs, 1024, 204th meeting, 2003.

[5]. Othman, M.H.D.; Ismail, A.F.; Mustafa, A.; “ Physico-chemical study of sulfonated Poly (ether ether ketone) membranes for Direct Methanol Fuel Cell applications” *Malaysian polymer journal (MPJ)*, vol 2 (2007): 10 -28.

[6]. Beer, L.; Olmeijer, D.L.; Lefebvre, M.C. “Simultaneous measurement of proton conductivity and methanol permeability for the development of Direct Methanol Fuel Cell Membranes” *PolyFuell Inc, Califonia*.

[7]. Eco Chemie B.V. “Supercapacitors: Principles and characterization using Autolab”, www.autolab-instruments.com.

[8]. Trassatti, S.; Kurzweil, P.; *Platinum Metals Rev.*, 38 (1994):46-56.

[9]. Zheng, J.P.; Jow, T.R.; J. *Electrochem. Soc.*, 142 (1995).

[10]. Sarangapani, S.; Lessner, P.M.; LaConti, A.B.; *U.S. Patent 5 136 474* (1992).

[11]. Sarangapani, S.; Tilak, B.V.; Chen, C.P. *J. Electrochem. Soc.*, 143 (1996).

[12]. Burke, A. "Ultracapacitors: why, how, and where is the technology." *J. Power Sources*, 91 (2000): 37 - 50

[13]. Mehrer, H. " Diffusion in Solids: Fundamentals, Method, Materials, Difusion – Controlled Processes" *Springer*, 2007.

[14]. Choi, J.; Kim, H.D.; Kim, K.H.; Shin, C.; Kim, C.S. "Polymer blend membranes of sulfonated poly(arylene ether ketone) for direct methanol fuel cell." *Journal of membrane science* 310 (2008): 384 – 392.

[15]. Zhu, J. G. 'Super Capacitors' University of Technology, Sydney.

[16]. http://commons.wikimedia.org/wiki/File:Activated_Carbon.jpg

[17]. http://rmn.iqfr.csic.es/guide/man/beginners/chap3-9.htm

Chapter 2

Solid State NMR

2.1 Basic Concepts

Magnetic nuclei possess an intrinsic angular momentum *I*, known as spin, with magnitude given by $[I(I+1)]^{\frac{1}{2}}\hbar$ [1, 2]. Because of the proportional relation between the spin angular momentum and the magnetic moment $\boldsymbol{\mu}$ given by $\boldsymbol{\mu} = \gamma \boldsymbol{I}$ [3,4], where the proportionality constant γ is called the nuclear gyromagnetic ratio, nuclear energy levels are non-degenerate when a magnetic field is present.

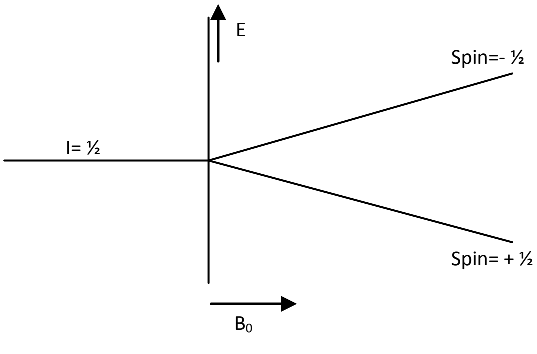

Figure 2.1: Removal of non-degeneracy of spin-1/2 nucleus in a magnetic field B_0

This can be seen through the classical energy expression; $E = -\boldsymbol{\mu}.\boldsymbol{B}$, where the magnetic field direction is taken along the z-direction. Then $E = -\mu_z B_0$, where μ_z is the z component of $\boldsymbol{\mu}$ and $\mu_z = \gamma I_z$. Since $I_z = m\hbar$, the magnetic energy levels are quantized such that: $m = I, I-1, I-2, \ldots. -I+1, -I$ and the energy of a state can be written as $E = -m\hbar\gamma B_0$. In this way the energy difference between two adjacent levels is $\hbar\gamma B_0$. Transition probabilities for $\Delta m = \pm 1$ are overwhelmingly large relative to multiple quantum transitions, and correspondingly, typical nuclear magnetic resonance (NMR) experiments yield energies very near $\hbar\gamma B_0$ [1]. By exposing a nuclear magnetic moment in the presence of a magnetic field to a 'pulse' of electromagnetic radiation of the proper frequency (typically on the order of radio frequencies or rf), the nuclear energy state can transit from a lower to next higher state. The transition energy is therefore written as:

$\Delta E = h\nu = \hbar\gamma B_0$ and the magnitude of the frequency (called the Larmor frequency) is given by

$$\nu = \frac{\gamma B_0}{2\pi} \text{ or } \omega_0 = \gamma B_0 \qquad (2.1)$$

This frequency can also be viewed as a precession frequency, i.e. the angular rate of the precession that nuclear magnetic moment makes about the magnetic field direction. The precession sense can be either clockwise or counter clockwise depending on the sign of γ. This phenomenon along with the magnitude of γ is nucleus specific.

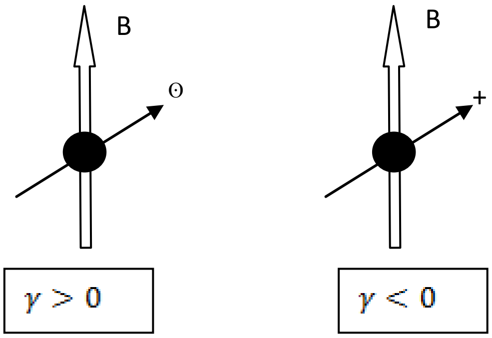

Figure 2.2: Clockwise and counter clockwise rotations: Θ-out of the page and +-into the page

When an ensemble of interacting nuclear moments is placed in a magnetic field, the system will come to equilibrium in such a way that the energies become distributed amongst the $2I+1$ energy states. This is a thermodynamic argument where the Boltzmann distribution typically describes the phenomenon. For example, if $I = ½$, then two non-degenerate magnetic energy levels will be populated with n_{upper} nuclei in the higher level and n_{lower} nuclei in the lower level, and the Boltzmann distribution can be written as $\frac{n_{upper}}{n_{lower}} = e^{-\frac{\Delta E}{kT}}$, [7][8] where k is the Boltzmann constant and T is the sample absolute temperature. At room temperature, the population difference ($n_{lower} - n_{upper}$) is typically ~ 10^{-6}. The population difference can be increased by decreasing the temperature of the sample or increasing strength of the external magnetic field.

2.2. Semi-classical description

When an ensemble of spin ½ nuclei is placed in a magnetic field (**B**), the system comes to equilibrium as a net magnetization (***M***) is built along the external magnetic field (***B***) direction according to the Boltzmann distribution. How this macroscopic magnetization behaves after applying a RF pulse to force an energy transition can be described classically by the equation of motion of the nuclear spin magnetization, known as the Bloch equation [5, 6].

$$\frac{d\boldsymbol{M}}{dt} = \gamma \boldsymbol{M} \times \boldsymbol{B}. \qquad (2.2)$$

It is seen that the direction of change of the magnetization is perpendicular to both the magnetization and the external field; hence there is a precession of the magnetization about the external field. As previously mentioned, the rate of precession is given by the Larmor frequency, $\omega_0 = \gamma B_0$. A resonance experiment can be implemented through application of a pulsed transverse magnetic field ($\boldsymbol{B_1}$) oscillating at ω_0. This field will bring about the excitation needed to shift the populations between lower and upper energy states.

Since the magnetization precesses about the static magnetic field B_0 at ω_0, it is instructive to envision a rotating frame of reference where B_1 is effectively stationary and the external magnetic field is zero. In this way, rotation of the magnetization about B_1 can be produced by applying the excitation pulse for a limited period of time, *t* [3].

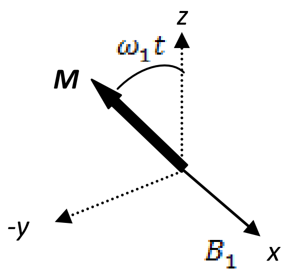

Figure 2.3: Magnetization rotation about the rf-field

The effect of a radiofrequency pulse is to tilt the equilibrium magnetization by an angle (flip angle, θ) , $\omega_1 t$, where *t* is the pulse length. This time can be chosen to make the flip angle θ equal to $\frac{\pi}{2}$ where maximum excitation of transverse magnetization is possible, or π, where the equilibrium magnetization is inverted.

For example, in order to flip the equilibrium magnetization by $\frac{\pi}{2}$ onto the xy plane, the excitation pulse is applied along x-axis, whereby the magnetization initially along the z-axis is rotated along -y-axis. Immediately after the pulse there is no more rf excitation and the populations are equal. The state of the system at this point is referred to as a coherence. In the laboratory frame the x-y plane magnetization coherence precesses at the Larmor frequency; however not forever, since ***M*** eventually returns to thermal equilibrium along the z-axis as governed by the Boltzmann distribution. This process is known as spin-lattice relaxation or longitudinal relaxation and the characteristic time for relaxation, which can be measured in an NMR experiment, is called spin-lattice relaxation time T_1. As the name implies, there is a net exchange of energy between the spin system and the surrounding thermal reservoir (lattice) until the system reaches equilibrium. Using the Bloch formulation of eqn. (2.2), the following phenomenological expression describes the evolution of M_z under spin-lattice relaxation [3, 5, 6].

$$\frac{dM_z}{dt} = -\frac{M_z - M_0}{T_1} \qquad (2.3)$$

The solution to (2.3) with physically appropriate boundary conditions is

$$M_z(t) = M_0(1 - \exp\left(-\frac{t}{T_1}\right)) \qquad (2.4)$$

The coherences (planar components of ***M***: M_x and M_y) also evolve in time as dictated by relaxation processes. Even though longitudinal relaxation influences the evolution of the coherences to a small degree, the relaxation of the coherences (transverse relaxation) is characterized primarily by homonuclear and heteronuclear magnetic dipole or spin-spin interactions between neighboring nuclei. In analogy with longitudinal relaxation, transverse relaxation also has a characteristic time (T_2) that specifies the lifetime of the coherences, i.e. the characteristic time required for the coherences to dephase. Again, as inferred from eqn. (2.2), the phenomenological description for transverse relaxation may be written as:

$$\frac{dM_{tran}}{dt} = -\frac{M_{tran}}{T_2} \qquad (2.5)$$

where M_{tran} is either M_x or M_y. The solution to above equation in the laboratory frame is [6]:

$$M(t) = (M_0 \cos\omega_0 t\,\hat{\imath} + M_0 \sin\omega_0 t\,\hat{\jmath}) exp(-\frac{\mathrm{t}}{\mathrm{T_2}}). \quad (2.6)$$

In a typical NMR experiment, the signal that is measured following a rf pulse is the superposition of coherences as a function of time.

2.3 Fundamental Interactions for Condensed Matter

2.3.1 Dipolar coupling

Every nucleus that has non-zero spin quantum number possesses a magnetic dipole moment (μ). The classical expression for the magnetic interaction energy between two nuclei can be written as [3]:

$$E = \frac{\mu_0}{4\pi}\left(\frac{\bar{\mu}_1 . \bar{\mu}_2}{r^3} - 3\frac{(\bar{\mu}_1 . \bar{r})(\bar{\mu}_2 . \bar{r})}{r^5}\right) \qquad (2.7)$$

where $\boldsymbol{r}$ is the radius vector from $\bar{\mu}_1$ to $\bar{\mu}_2$. Quantum mechanically, the nuclear dipole moments are written in terms of the corresponding spin operators.

$$\bar{\mu}_1 = \gamma_1 \hbar I_1 \text{ and } \bar{\mu}_2 = \gamma_2 \hbar I_2$$

In order to consider all nuclear dipolar interactions within the system, the dipolar Hamiltonian operator can be employed.

$$H_D = \frac{\mu_0 \hbar^2}{4\pi}\left(\frac{1}{2}\right)\sum_{j=1}\sum_{k=1}\gamma_j\gamma_k\left(\frac{\overrightarrow{I_j}.\overrightarrow{I_k}}{r_{jk}^3} - 3\,\frac{(\overrightarrow{I_j}.\bar{r})(\overrightarrow{I_k}.\bar{r})}{r_{jk}^5}\right) \quad (2.8)$$

The dipolar interaction is typically much smaller than the Zeeman interaction and therefore first-order perturbation theory in which I_z is diagonal can be used. The secular dipolar Hamiltonian is given below [7].

$$H_{Dsec} = \frac{\mu_0\gamma^2\hbar}{4\pi}\frac{1}{2}\sum_{j<k}\frac{1}{r_{jk}^3}\left(1 - 3\cos^2\theta_{jk}\right)[3I_{zj}I_{zk} - \mathbf{I_j}.\mathbf{I_k}] \quad (2.9)$$

where I_z is the component of the spin along the direction of the external field, and θ_{jk} is the angle between the external field $\boldsymbol{B}_0$ and the vector $\boldsymbol{r}_{jk}$. The dipole-dipole interaction, which arises from the interaction of magnetic nuclei, be they the same type or different, either through the molecule (intramolecular) or between molecules (intermolecular). It is a through-space interaction. Dipole-dipole interaction is a short-range interaction since it falls off as the inverse of the distance between the dipoles cubed. The strength of this interaction depends on the relative orientation of the dipoles as well as the distance between them. In solid systems the nuclear distances are fixed therefore these interactions are not averaged out and can dominate the spectra. However it is only the secular (diagonal) terms which commute with the Zeeman Hamiltonian.

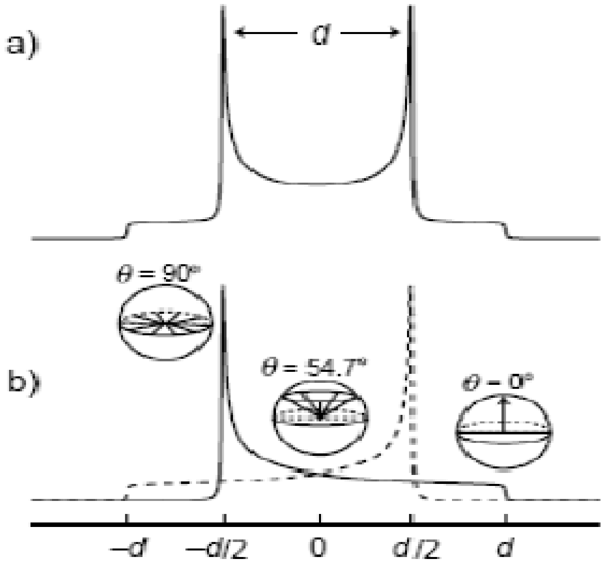

Figure 2.4: a). Powder pattern of dipolar coupling, b). Arising of fake doublets [16].

Figure 2.4 elucidates how orientations of nuclear dipoles yield the broad NMR spectrum. As seen, in a powder there is lot of spins and they have a large number of different orientations leading to a broad spectrum.

2.3.2 Chemical Shift

The NMR frequency $\omega = \gamma B$ depends not only on the applied magnetic field ($\boldsymbol{B}_0$) but also on the local magnetic field ($\boldsymbol{B}_{\text{loc}}$) due to the susceptibility of the medium at the position of the nucleus. This local magnetic field augments (opposites) the external field such that, $\boldsymbol{B} = \boldsymbol{B}_0 + \boldsymbol{B}_{\text{loc}}$ ($\boldsymbol{B} = \boldsymbol{B}_0 - \boldsymbol{B}_{\text{loc}}$). Thus, the resonance frequency is shifted from the Larmor frequency. This effect is generally called the chemical shift when it arises from electronic current distributions, although the true nature of the underlying physics may arise from any number of additional interactions including electron-nucleus contact interactions, core-electron polarization effects and paramagnetism [4,7]. If electronic currents produce magnetic fields opposite to $\boldsymbol{B}_0$ as in diamagnetic materials, then the resultant field $\boldsymbol{B}$ is slightly lower than $\boldsymbol{B}_0$, and the NMR frequency is lower than the Larmor value. The term ‘nuclear shielding’ is used to describe the relative negative shift, while ‘deshielding’ is used for relative positive shifts. In the solid-state, the local field arising from electron current distributions can be thought of as due to an intrinsic magnetic susceptibility for the medium. It follows that the chemical shift be regarded as a tensor quantity. Therefore, the resultant induced magnetic field is related to the applied magnetic field through the chemical shift tensor $\overline{\boldsymbol{\sigma}}$.

$$\boldsymbol{B}_{\boldsymbol{shifted}} = -\overline{\boldsymbol{\sigma}}.\boldsymbol{B}_{\boldsymbol{0}}$$

Then, the chemical shift Hamiltonian is:

$$\begin{aligned} H_{CS} &= -\boldsymbol{\mu}.\boldsymbol{B}_{\boldsymbol{shifted}} \\ &= \boldsymbol{\mu}.\overline{\boldsymbol{\sigma}}.\boldsymbol{B}_{\boldsymbol{0}} \qquad (2.10) \end{aligned}$$

where:

$$\sigma = \begin{pmatrix} \sigma_{11} & \sigma_{12} & \sigma_{13} \\ \sigma_{21} & \sigma_{22} & \sigma_{23} \\ \sigma_{31} & \sigma_{32} & \sigma_{33} \end{pmatrix}$$

The diagonalized chemical shift tensor components are typically quoted in the literature. NMR studies of the chemical shift tensor in single-crystal solids require that the orientation of the chemical shift principal axis be specified relative to $\boldsymbol{B}_{\boldsymbol{0}}$. In this case, it is observed that the NMR frequency depends on the orientation of the chemical shift tensor in the principle axis system (PAS).

$$\begin{tikzcd} \sigma = \begin{pmatrix} \sigma_{11} & \sigma_{12} & \sigma_{13} \\ \sigma_{21} & \sigma_{22} & \sigma_{23} \\ \sigma_{31} & \sigma_{32} & \sigma_{33} \end{pmatrix} \arrow[r] & \sigma^{'} = \begin{pmatrix} \sigma^{'}_{xx} & 0 & 0 \\ 0 & \sigma^{'}_{yy} & 0 \\ 0 & 0 & \sigma^{'}_{yy} \end{pmatrix} \\ \text{As measured in the Lab Frame} \arrow[u] & \text{In the CSA PAS} \arrow[u] \end{tikzcd}$$

To see this, consider the 1st-order perturbation treatment for the $\Delta m = -1$ transition under the chemical shift interaction [4]:

$$\nu = \upsilon_0(1 - \sigma^{lab}{}_{zz})$$

Where $\sigma^{lab}{}_{zz}$ is the chemical shift tensor component along the direction of $\boldsymbol{B}_0$. The use of rotation matrices $R_y(\theta)$ and $R_z(\phi)$ allows for σ' to be transformed into the lab frame:

$$\sigma_{lab} = R_y^{-1}(\theta)R_z^{-1}(\phi)\sigma' R_z(\phi)R_y(\theta)$$

$$\sigma^{lab}{}_{zz} = \sin^2\theta\,(\sigma'_{xx}\cos^2\phi + \sigma'_{yy}\sin^2\phi) + \sigma'_{zz}\cos^2\theta \qquad (2.11)$$

Then

$$\nu = \upsilon_0(1 - \sin^2\theta\,(\sigma'_{xx}\cos^2\phi + \sigma'_{yy}\sin^2\phi) - \sigma'_{zz}\cos^2\theta)$$

The above expression may be simplified further as:

$$v = v_0(1 - (\sigma_{iso} + \sigma_{aniso}\,(3\cos^2\theta - 1) + \sigma_{aniso}\,.\,\eta_{cs}\sin^2\theta\cos 2\phi) \qquad (2.12)$$

where $\sigma_{iso} = \frac{1}{3}(\sigma'_{xx} + \sigma'_{yy} + \sigma'_{zz})$, $\sigma_{aniso} = \frac{2\sigma'_{zz} - \sigma'_{yy} - \sigma'_{xx}}{3}$ and $\eta_{CS} = \frac{\sigma'_{yy} - \sigma'_{zz}}{\sigma'_{xx} - \sigma'_{iso}}$.

σ_{aniso} is the anisotropic constant which can be removed by the MAS technique and η_{CS} is the asymmetry parameter [9]. The axial symmetry anisotropy is given as:

$$\zeta = 2\left(\frac{\sigma_{yy} - \sigma_{xx}}{\sigma_{zz} - \sigma_{xx}}\right)$$

For polymers, glasses and in general amorphous and polycrystalline systems, all orientations (specified by polar angle θ and azimuthal angle ϕ) are realized and the NMR spectrum is a chemical shift anisotropy powder pattern (CSA) as illustrated in figures 2.5.a and 2.5.b for the cases of asymmetric and axially symmetric anisotropies.

a

b

Figure 2.5: Chemical-shift powder pattern for a). Asymmetric anisotropy and b). Axially symmetric anisotropy

In practice, the isotropic chemical shift δ_{iso} is quoted in units of part-per-million (ppm) and measured relative to that of a reference compound v_{ref}, as follows [1]:

$$\delta_{iso} = 10^6\left(\frac{v - v_{ref}}{v_{ref}}\right)\text{ppm} \qquad (2.13)$$

δ_{iso}, unlike frequency quoted in Hz, is dependent solely on the system being investigated and is independent of the external magnetic field.

2.3.3 Nuclear Electric Quadrupole Interaction

The quadrupolar interaction is an interaction between the electric quadrupole moment of a nuclear spin $I \geq 1$ and the electric field gradient surrounding it. There is no quadrupolar interaction for spin -1/2 nuclei.

Quadrupolar Hamiltonian in PAS is:

$$H_q = \frac{eQ}{4I(2I-1)}\left[V_{zz}\left(3I_{z(PAS)}^2 - I^2\right) + \left(V_{xx} - V_{yy}\right)\left(I_{x(PAS)}^2 - I_{y(PAS)}^2\right)\right] \quad (2.14)$$

Where Q is the quadrupole moment, I is the spin angular momentum. The term $V_{\alpha\beta}$ $(\alpha, \beta = x, y, z)$ is the electric field gradient (EFG) and:

$$V_{\alpha\beta} = 0 \; if \; \alpha \neq \beta$$

The above property necessarily means that off-diagonal terms are zero in the principle axis system (PAS).

$$V = \begin{pmatrix} V_{xx} & 0 & 0 \\ 0 & V_{yy} & 0 \\ 0 & 0 & V_{zz} \end{pmatrix}$$

The above equation can be written using the field gradient and the asymmetry parameter.

$$eq = V_{zz}$$

$$\eta = \frac{(V_{xx} - V_{yy})}{V_{zz}}$$

The below Hamiltonian should be transformed into the LAB frame as the Zeeman interaction is in the lab frame.

$$H_q = \frac{e^2qQ}{4I(2I-1)}[(3I_{z(PAS)}^2 - I^2) + \eta(I_{x(PAS)}^2 - I_{y(PAS)}^2)]$$

Transformation can be done by rotating angular momentum operates as below [10]:

$$\begin{pmatrix} \hat{I}_x \\ \hat{I}_y \\ \hat{I}_z \end{pmatrix} = R(\theta,\phi) \begin{pmatrix} \hat{I}_{x\,PAS} \\ \hat{I}_{y\,PAS} \\ \hat{I}_{z\,PAS} \end{pmatrix}$$

Then quadrupole Hamiltonian is in the LAB frame is:

$$\widehat{H}_Q = \frac{e^2qQ}{4I(2I-I)\hbar}\bigg\{\frac{1}{2}(3\cos^2\theta - 1)(3\hat{I}_z^2 - \hat{I}^2) + \frac{3}{2}\sin\theta\cos\theta\,[\hat{I}_z(\hat{I}_+ + \hat{I}_-)\hat{I}_z] +$$

$$\frac{3}{4}\sin^2\theta\,(\hat{I}^2{}_+ + \hat{I}^2{}_-)\bigg\} + \eta_Q\frac{e^2qQ}{4I(2I-1)\hbar}\bigg\{\frac{1}{2}\cos 2\phi\,[(1 - \cos^2\theta)(3\hat{I}_z^2 - \hat{I}^2) + (\cos^2\theta +$$

$$1)(\hat{I}_+^2 + \hat{I}_-^2)] +$$

$$\frac{1}{2}\sin\theta\cos 2\phi - i\sin 2\phi)(\hat{I}_+\hat{I}_z + \hat{I}_z\hat{I}_+) + (\cos\theta\cos 2\phi + i\sin 2\phi)(\hat{I}_-\hat{I}_z + \hat{I}_z\hat{I}_-) +$$

$$\left(\frac{i}{4}\right)\sin 2\phi\cos\theta\,(\hat{I}_+^2 - \hat{I}_-^2)\bigg\} \qquad (2.15)$$

Perturbation theory can be used to find the energy correction to the Zeeman energy levels as Zeeman energy is significantly large. The first order and the second order corrections are shown below.

$$E_m^1 = \frac{e^2qQ}{4I(2I-1)}(I(I+1) - 3m^2)\left[\frac{1}{2}(3\cos^2\theta - 1) - \eta\cos 2\phi\,(\cos^2\theta - 1)\right] \qquad (2.16)$$

where m is the magnetic quantum number, and θ and ϕ are the polar and azimuthal angles specifying the orientation of the EFG principal axis. Clearly, there is no 1st-order quadrupolar interaction for the central transition (m = 1/2). In the case of axially symetry, $\eta = 0$. Then at the $\theta = 54.7^0$, The first order term becomes zero. Therefore, MAS is a excellent technique to harvest valuable information of quadrupole nuclei when axially symetry is present.

As can be seen, the first term in the second order correction does not have any angular dependant term. That means it is isotopic. The other observation is that second order correction depends on the inverse of the Larmor Frequency. Therefore, high field NMR does not have a significant contribution from the second order.

$$E_m^2 = -\left(\frac{e^2qQ}{4I(2I-1)}\right)^2\left(\frac{m}{\omega_0}\right)\Big\{-\frac{1}{5}(I(I+1)-3m^2)\left(3+\eta_Q^2\right)+\frac{1}{28}(8I(I+1)-12m^2-3)\left[\left(\eta_Q^2-3\right)(3\cos^3\theta-1)+6\eta_Q\sin^2\theta\cos 2\phi\right]+\frac{1}{8}(18I(I+1)-34m^2-5)\left[\frac{1}{140}(18+\eta^2)(35\cos^4\theta-30\cos^2\theta+3)+\frac{3}{7}\eta_Q\sin^2\theta\,(7\cos^2\theta-1)\cos 2\phi+\frac{1}{4}\eta_Q^2\sin^4\theta\cos 4\phi\right]\Big\} \qquad (2.17)$$

2.4 **Relaxations**

The equilibrium magnetization is perturbed in performing an NMR experiment by applying a RF pulse. To repeat the experiment again, the equilibrium must once again achieved and the return to the equilibrium occurs via processes known as relaxation.

Restoration of the magnetization along the external magnetic field is called longitudinal magnetization and in this process energy is exchanged between spin and the lattice. Therefore this relaxation process is called spin-lattice relaxation and time taken for this process is known as spin lattice relaxation time T_1. The magnetization in the x-y plane restores to its equilibrium value, which is zero, within the characteristic time constant spin-spin relaxation T_2. This process doesn't involve any energy exchange between spins and the surrounding. Spin-lattice relaxation time in the rotating frame of reference is indicated by $T_{1\rho}$. To obtain $T_{1\rho}$ value the magnetization is locked in the x-y plane such that the magnetization and the applied field, B_1, rotate together. Then relaxation process occurs in the direction of B_1.

Energy exchange in these relaxation processes is stimulated by fluctuations in the local magnetic field generated by dipolar coupling, quadrupolar coupling, chemical shift anisotropy, spin rotation and scalar coupling. Stronger interactions lost to faster relaxation for a given frequency spectrum of the motion. Fluctuation of local magnetic field in terms of frequency is given by the spectral density $J(\omega)$.

$$J(\omega) = \frac{\tau_c}{1+\omega^2\tau_c^2} \qquad (2.18)$$

The spectral density is the Fourier transform of the autocorrelation function describing the fluctuating magnetic fields. The autocorrelation function may be written as

$G(t) \propto h(t).h(0) \propto \exp\left(-\frac{t}{\tau_c}\right)$. This expression means the probability of finding a correlation between the local field at time t and t=0 decreases as $\exp\left(-\frac{t}{\tau_c}\right)$. Therefore τ_c is called the correlation time. h(t) and h(0) are the same local field at two different times. To obtain the above spectral density, Fourier transformation of the correlation function can be taken as follow.

$$J(\omega) = \int_{-\infty}^{\infty} G(t)\exp(-i\omega t)\,dt \qquad (2.19)$$

At a given frequency spectral density depends on the correlation time, τ_c which typically has Arrhenius temperature dependence.

Fluctuations of magnetic and electric fields at the nuclear sites strongly influence the relaxation. According to the BPP theory (Bloembergen, Pound and Purcell, 1948 and Bloembergen, 1961) ionic motions are random and T_1 is given by:

$$\frac{1}{T_1} = C[J(\omega) + 4J(2\omega)] \qquad (2.20)$$

Where C is a constant determined by the specific time varying interaction.

For examples

$C = \left(\frac{\mu_0}{4\pi}\right)^2 \left(\frac{2\gamma^4\hbar^2 I(I+1)}{5r^6}\right)$ for homonuclear dipolar relaxation and

$C = \frac{3}{40}\frac{2I+3}{I^2(2I-1)}\left(1+\frac{\eta^2}{3}\right)\left(\frac{eQ}{\hbar}\frac{\partial^2 V}{\partial z'^2}\right)^2$ for Quadrupolar relaxation.

There is a minimum in the graph of T_1 vs. *1/T* which occurs when $\omega_0\tau_c = 1$ as shown in figure 2.6.

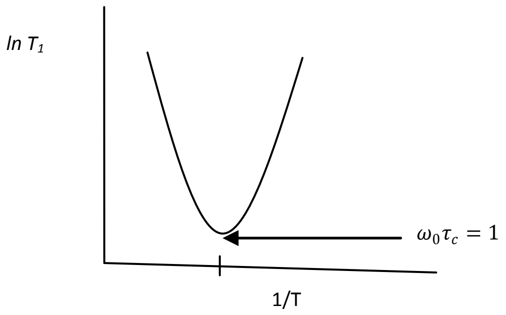

Figure 2.6: T_1 vs. *1/T*

T_2 and $T_{1\rho}$ are also related to spectral density as follow.

$$\frac{1}{T_2} = C'[3J(0) + 5J(\omega) + 2J(2\omega)] \quad (2.21)$$

$$\frac{1}{T_{1\rho}} = C'[3J(\omega) + 5J(\omega) + 2J(2\omega)] \quad (2.22)$$

For homonuclear dipolar coupling:

$$C' = \left(\frac{\mu_0}{4\pi}\right)^2 \left(\frac{\gamma^4\hbar^2 I(I+1)}{5r^6}\right)$$

When ionic motions are thermally activated, correlation time is given by $\tau_c = \tau_0 \exp(\frac{E_A}{k_B T})$, where E_A is the activation energy, k_B is the Boltzmann constant, and T is the temperature.

2.5 **Magic Angle Spinning**

Examination of the 1^{st}-order energy contributions from the dipolar, chemical shift, and quadrupolar Hamiltonians, equations 2.9, 2.12, and 2.16 respectively, reveal the dependences on the PAS orientations as specified by θ and ϕ. It is noted that not all three interactions need be present, and that their respective principal axes need not be coincident. The complex resultant solid-state NMR lineshape in general will be the superposition of resonant frequencies as specified by angles θ and ϕ. The observed lineshape is a mixture of powder patterns characterized by broad and heterogeneous features.[9]

A very nice way to simplify the solid-state NMR powder pattern when the above broadening interactions are present, is to perform an average over the orientations θ and ϕ. This can be achieved through rapid rotation of the sample about an angle that makes any or all of the angular parts of the Hamiltonian zero. For example, the dipolar energy (eqn. 2.9), the CSA (eqn 2.12) and the 1^{st}-order quadrupolar energy (eqn. 2.16) all contain $(3\cos^2\theta - 1)$ terms. These various energy contributions can be reduced or made to vanish altogether when the sample itself is rapidly rotated about an axis oriented at $\theta = 54.7^0$ relative to the $\boldsymbol{B}_0$ direction (the magic angle).

The effect of MAS on a NMR spectrum is shown in figure 2.6. At high spinning rates for samples that have only dipolar and CSA interactions (and small quadrupole interactions) a simple narrow line is observed at a frequency position of the isotropic chemical shift (δ_{iso}). Also, if the spinning speed is lower than the static linewidth, then incomplete angular averaging occurs and additional peaks called sidebands will be present [10].

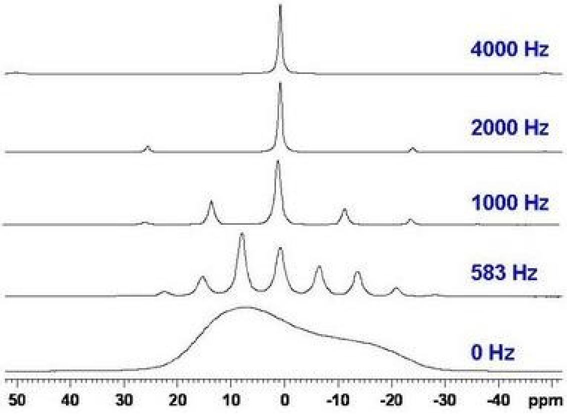

Figure 2.7: Effect of Magic Angle Spinning, resolution depends on the spinning speed [17].

2.6 NMR Pulse Sequences

The NMR experiments in this thesis were conducted using two spectrometers: a modern (2007) wide bandwidth pulsed spectrometer, built by Varian Inc. and a Chemagnetics 300 CMX broadband spectrometer. As was mentioned at the beginning of this chapter, the pulse sequence manipulates the nuclear spins most generally by: 1) *preparation*, 2) *excitation*, 3) *evolution*, and 4) *detection*. In this section, each pulse sequence used in the thesis is summarized.

2.6.1 Single Pulse

The single-pulse measurement (figure 2.8) is the simplest pulse sequence to obtain an NMR spectrum. It primarily rotates the sample magnetization from +**z** (along

$\boldsymbol{B}_0$ at equilibrium) into the –**y** direction by the action of a $\frac{\pi}{2}$ pulse (see section 2.2). To prevent saturation, the spin system is *prepared* at equilibrium by waiting a period of time (recycle delay ~ 7 x T_1) prior to the high-power radio frequency (rf) *excitation* pulse. After the $\frac{\pi}{2}$ pulse, the sample magnetization freely *evolves* within the x-y plane as it precesses about $\boldsymbol{B}_0$ (and decays with a characteristic time of T_2) and recovers along **z** towards its equilibrium value (with a characteristic time of T_1).

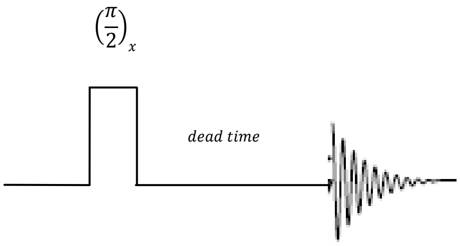

Figure 2.8: Single Pulse Sequence

The NMR receiver detects magnetization during the *evolution* period within the x-y plane, and as described earlier this signal is processed and transformed into the NMR spectrum. Differentiating magnetization generated by the pulse and sample is crucial; therefore as a practical matter, time must be allowed for the receiver electronics to recover after application of the high-power pulse, in order to detect signal from the sample only. This time period is called 'deadtime' and is typically about 10 to 20 μs. Any freely evolving sample magnetization within the deadtime is considered lost since it cannot be recovered without knowledge of the spectrometer electronics recovery profile.

2.6.2 Spin Echo

One approach to get around the spectrometer deadtime issue is to refocus the sample magnetization such that it begins its evolution beyond the deadtime. In the spin-echo [11], as shown in figure 2.9, the $\left(\frac{\pi}{2}\right)_x$ pulse rotates the equilibrium magnetization onto x-y plane whereby it freely dephases during the time τ. At this point a π_y pulse is applied which rotates the dephased magnetization 180° and leads to the coherent refocusing of spins (echo).

Another application of the spin-echo pulse sequence is in studying transverse relaxation; which is primarily responsible for the evolution of the planar magnetization components. A rough measure of the spectral full-width-at-half-maximum (FWHM) in the case of homogeneous broadening interactions is given by $\frac{1}{\pi T_2}$ where T_2 is the intrinsic transverse relaxation time [4, 9]. But, usually there is a spatial inhomogeneity over the sample and it is responsible for inhomogeneous broadening. As a result there are two broadening mechanisms, homogeneous and inhomogeneous, and therefore a new transverse relaxation time constant, T_2*, should be introduced. T_2^* is related to the intrinsic transverse relaxation time constant T_2 and inhomogeneity of the field through

$$\frac{1}{T_2{}^*} = \frac{1}{T_2} + \gamma \Delta B_0. \quad (2.23)$$

The spread in Larmor speed $\gamma \Delta B_0$ is due to the field inhomogeneity ΔB_0. If the inhomogeneity of the external magnetic field is fairly large, then it is not possible to obtain much information about the sample. The spin-echo pulse sequence introduced by

Erwin Hahn in 1950 [11] can be used to measure T_2 as the inhomogeneous broadening is removed by refocusing of spins [6,9].

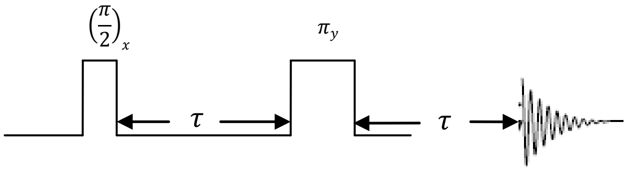

Figure 2.9: Spin echo pulse sequence

Again referring to fig. 2.9, following the $\left(\frac{\pi}{2}\right)_x$ pulse, the magnetization freely dephases during the time τ. As the dephasing time is allowed to increase, there will be a smaller coherent signal within the x-y plane due to transverse relaxation processes. Since the goal is to study the amplitude of the coherence as a function of τ, the remnant magnetization is refocused through the application of a π_y pulse to create an echo while simultaneously reversing the inhomogeneous part of the signal decay so that it does not contribute to the acquired signal. The NMR signal intensity, a solution of eqn. 2.5, is given by exponential expression (2.24) as a function of τ with characteristic time constant, T_2.

$$M(2\tau) = M(0)e^{-\frac{2\tau}{T2}} \qquad (2.24)$$

2.6.3 Inversion Recovery

This pulse sequence is used to measure the spin-lattice relaxation time, T_1. After the spin system is prepared at equilibrium (during the recycle delay time), the spin magnetization is inverted into the –z direction through application of a π pulse as shown in fig. 2.10 [4, 9].

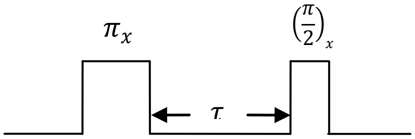

Figure 2.10: Inversion Recovery Pulse Sequence

During the evolution time τ , the inverted magnetization recovers along the +z-axis towards its equilibrium value of M_0. A longer evolution time allows for the system to approach M_0 more closely. The goal is to monitor the recovered magnetization as a function of τ. In order to detect the recovering magnetization, a 90^0 pulse is applied along the x-axis which rotates $M_z(\tau)$ onto the y-axis. At this point, the free induction decay is recorded. The magnetization as a function of τ is given by eqn. 2.25 (similar to eqn. 2.4 but with different boundary conditions) and is illustrated in figure 2.11. T_1 can be extracted from the recovery profile.

$$M_z(\tau) = M_0\left(1 - 2e^{-\frac{\tau}{T_1}}\right) \qquad (2.25)$$

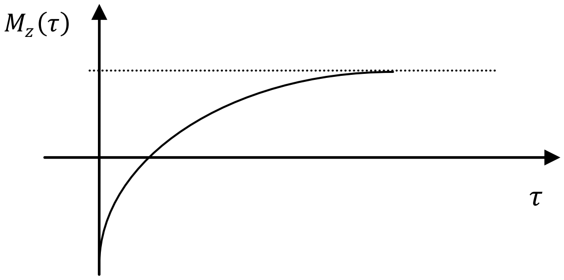

Figure 2.11: Magnetization vs. tau for Inversion Recovery

2.6.4 Saturation Recovery

Another way to measure spin-lattice relaxation time is to prepare the spin system in a saturated state and monitor its free evolution towards equilibrium. This approach has an advantage over inversion recovery in that it takes much less time to initially prepare the spins, provided the system can be saturated. Saturation recovery is the preferred method for the study of long T_1s (i.e. $T_1 > 10$ s).

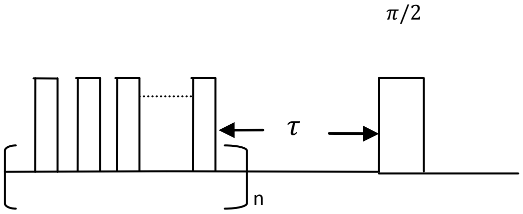

Figure 2.12 : Saturation comb

The saturated condition is created by subjecting the spin system to a rapid succession of saturation pulses. This pulse-train or 'comb' is typically comprised of 10 to 100 high-power $\pi/2$ or lower pulses separated by a delay greater than or on the order of T_2. After the spins are prepared in a saturated state, an evolution time τ is allowed for the spin system to evolve towards its equilibrium value of M_0. As with the inversion recovery sequence, the goal is to monitor the recovered magnetization as a function of τ.

The recovering magnetization is detected via application of a $\pi/2$ pulse. The magnetization as a function of τ is given by eqn. 2.26 (same as eqn. 2.4) and is illustrated in figure 2.12. T_1 can be extracted from the recovery profile.

$$M_z(\tau) = M_0\left(1 - \mathrm{e}^{-\frac{\tau}{T_1}}\right) \qquad (2.26)$$

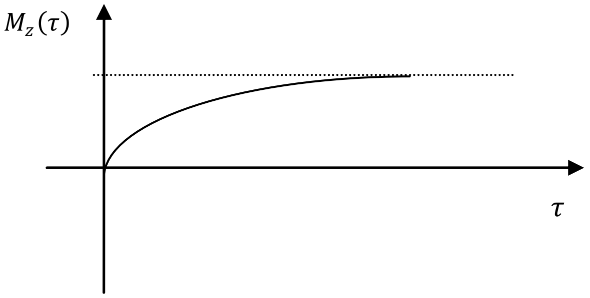

Figure 2.13: Magnetization vs. tau for Saturation Recovey.

2.6.5 Pulsed field gradient spin echo

In the spin echo experiment the echo formation is disturbed if there is any motion of the nuclei into different field regions or if the field varies in time. If this happens, then precession after π_y pulse no longer cancels exactly the precession before the pulse. The result is attenuation in the NMR signal. In other words, the signal from the spin echo experiment is not only dependent on T_1 and T_2, but also affected by the self diffusion of molecules experiencing magnetic field inhomogeneity. Therefore, one can use spin echo experiment in conjunction with the application of field gradients as a method of measuring the self diffusion coefficient.

Stejskal and Tanner (1964) [12] modified the Hahn echo pulse sequence with two gradient pulses instead of a steady state gradient. In a homogeneous field, nuclei precess at a constant Larmor frequency ω_0. The application of a magnetic field gradient, g, results in a spatial dependence of precession frequency which is given by $\omega_{eff} = \omega_0 + \gamma(\boldsymbol{g}.\boldsymbol{r})$. Where $\boldsymbol{g} = \frac{\partial B_z}{\partial x}\hat{\imath} + \frac{\partial B_z}{\partial y}\hat{\jmath} + \frac{\partial B_z}{\partial z}\hat{k}$ and $\hat{\imath}$, $\hat{\jmath}$, $\hat{k}$ are unit vectors in the x, y and z directions in the laboratory frame of reference. For diffusion measurements, the gradient is generally oriented along the z-axis parallel to B_0. The diffusion experiment monitors the change in precession frequency and the resulting phase shift of a nucleus as it moves from an original position to one where the field is slightly different.

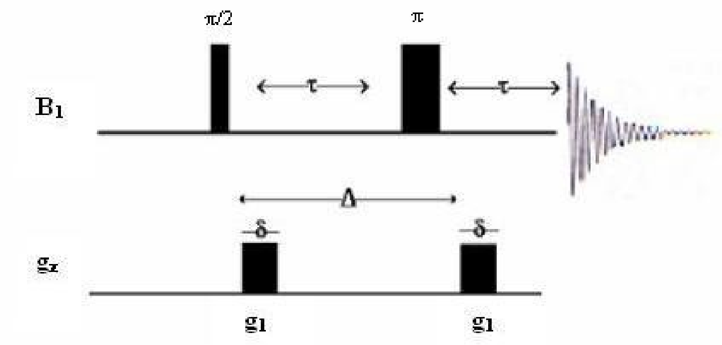

Figure 2.14: Pulsed field gradient spin echo pulse sequence

A typical pulse sequence is shown in Fig 2.13, where Δ is time between gradient pulses, g is gradient strength and δ is gradient pulse length. In this pulse sequence, the field gradients are applied after $\frac{\pi}{2}$ and π pulses. The effect of T_2 relaxation can be kept constant throughout the entire experiment by fixing τ and varying either the strength or duration of the gradient pulse. The $\frac{\pi}{2}$ pulse tips the magnetization onto the xy pulse. If diffusion occurs during the delay τ, the nuclei will experience a phase shift given by $\emptyset(t) = \gamma B_0 t + \gamma \int_0^t g(t')z(t')dt'$. The first term is due to the static field and the second term is due to the applied gradient. The observed echo attenuation is merely due to diffusion. The signal intensity is modeled with the equation given by:

$$A(g, 2\tau) = A(0,0) exp\left[-\gamma^2 g^2 D \delta^2 \left(\Delta - \frac{\delta}{3}\right)\right]. \qquad (2.27)$$

Where A(0,0) is the initial echo amplitude and A(g) is the attenuation echo amplitude. D is the self- diffusion coefficient [9]. D is obtained from performing the experiment with different g values and plotting *A(g)* versus *g*.

2.6.6 Pulsed field gradient Stimulated Echo

J.E. Tanner (1969)[13] pointed out the advantages of using stimulated echo for certain systems instead of PFGSE. This pulse sequence is useful when $T_1 > T_2$ where motion of molecules is slow compared with the period of the Larmor frequency [6].

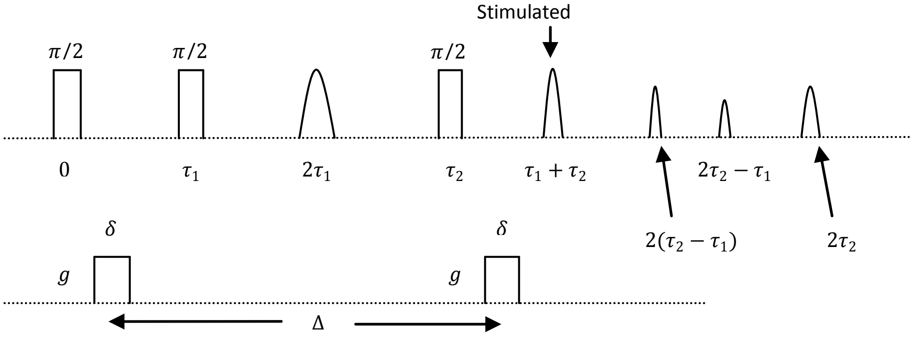

Figure 2.15: Stimulated echo pulse sequence

In the above figure, all rectangular shapes denote rf pulses and gradient pulses while non rectangular shapes referred to echoes. Hahn in 1950 [11] showed that five echoes could occur with this pulse sequence. The echo at $\tau_1 + \tau_2$ is called the stimulated echo. All three rf pulses have the same phase for example say phase is zero. This means the B_1 is applied along the x-axis. The first rf pulse flips the equilibrium magnetization into x-y plane and that magnetization dephases during time τ_1. At time τ_1 the second rf pulse is applied. The second rf pulse brings only the y component to the equilibrium state and hence half of the magnetization is restored. The x component is unaffected and it is responsible for the echo at $2\tau_1$. The third rf pulse is applied at τ_2 and it recalls the previously restored y-component of the magnetization to form the stimulated echo at $\tau_1 + \tau_2$. The other echoes are spin echoes. A spoiling gradient pulse can be applied between second and third rf pulse in order to prevent interference between spin echoes and stimulated echo. It is also possible to apply two filter gradient pulses to isolate fast decaying components from slow decaying components. The attenuation intensity is then given by [9]:

$$A(\tau_1 + \tau_2) = A(0)exp\left[-\gamma^2 D g^2 \delta^2 \left(\Delta - \frac{\delta}{3}\right)\right]. \qquad (2.28)$$

As seen, the above expression is same as for PFGSE. This pulse sequence is better for the systems such as viscous liquids, plastic crystals and system with quadrupolar coupling mentioned by J.E Tanner [13].

2.7 Solid Sate Diffusion Mechanisms

They are a number of possible ion transport mechanisms in crystalline solids. Conduction, which involves self-diffusion via Nernst-Einstein equation $\left(\sigma = \frac{Dq^2c}{kT}\right)$, of the host material will generally occur via a vacancy mechanism [14]. Vacancies are the sites where an atom or ion is absent. Therefore vacancy diffusion occurs via the migration of an atom from its own lattice site to an adjacent vacant lattice site as shown in the figure 2.16.

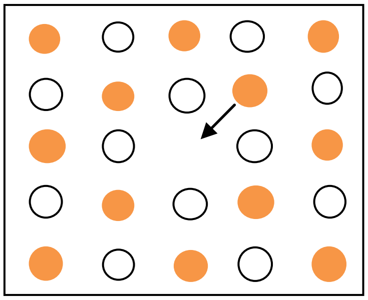

Figure 2.16: Vacancy Diffusion

The formation of vacancies is a thermally activated process described by the following equation.

$$N_v = Nexp\left(-\frac{E}{RT}\right) \quad (2.29)$$

where N_v is the number of vacancies, N is the total number of atomic sites, E is the activation energy for vacancies, R is the gas constant and T is temperature. Self-diffusion should readily occur in the presence of large vacancies. According to the equation (2.24), vacancies can be induced by increasing temperature as done in variable temperature (VT) NMR diffusion measurements.

Ion transport in solids can also occur via interstitial diffusion process [14] as shown in the figure 2.17.

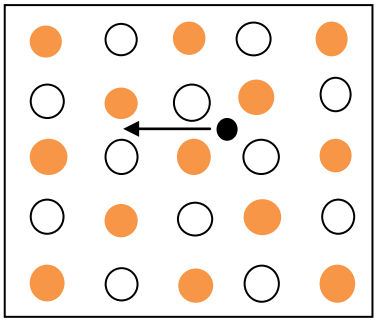

Figure 2.17: Interstitial diffusion

Interstitial sites are the voids that are not normally occupied in the crystal lattice and therefore diffusion occurs by migration of ions from one interstitial site to another. Interstitial diffusion should be more rapid than vacancy diffusion since the diffusing particles are smaller and there are more available interstitial sites than vacancies

For Polymer Electrolytes, the preferred diffusion mechanism will depend on the structure and the chemical nature of the membrane. Two main diffusion mechanisms cause transport of protons in electrolytes. They are the Grotthuss mechanism and Vehicular mechanism [15]. The Grotthuss mechanism is the mechanism by which an ‘excess’ proton or protonic defect diffuses through the hydrogen bond network of water molecules or other hydrogen bonded liquid through the formation / cleavage of covalent bonds. In other words it is the proton hops between hydrogen bonded water molecules.

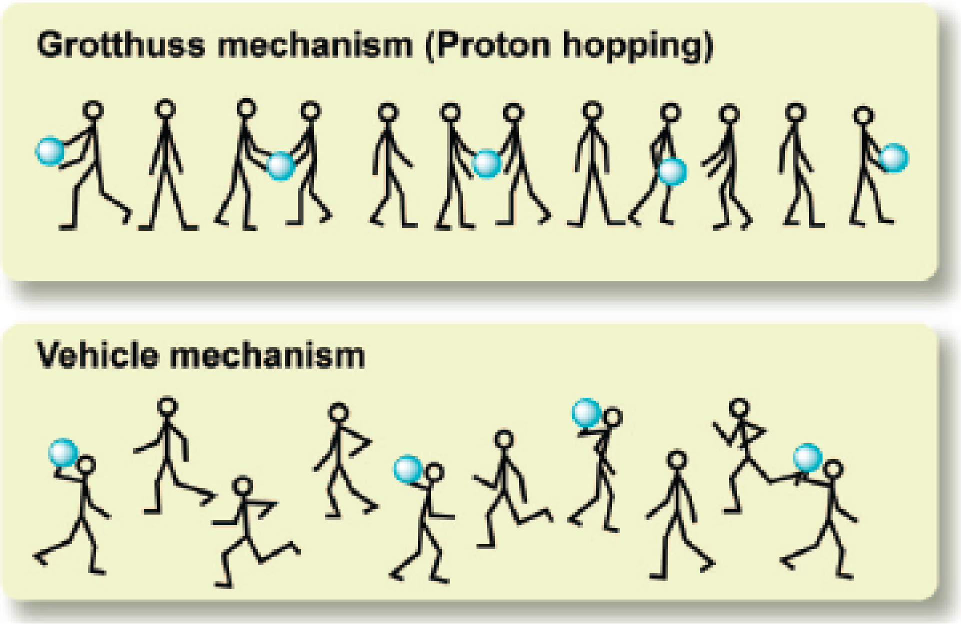

Grotthuss mechanism (Proton hopping)

Vehicle mechanism

Figure 2.18: Demonstration of the Grotthuss and Vehicle mechanisms [15].

Vehicle mechanism is the simple diffusion and migration of hydronium ions (H_3O^+).

References

[1]. Hore, P.J. “ Nuclear Magnetic Resonance” *Oxford* (2002).

[2]. Hore, P.J.; Jones, J.A.; Wimperis, S. “NMR: The Tookit” *Oxford* (2002).

[3]. Slichter, C.P. “Principle of magnetic resonance” *Happer and Row publishers* (1963).

[4]. Levitt, M.H. “Spin Dynamics” *John Wiley & Sons, LTD* (2005).

[5]. Abragam, A. “Principles of nuclear magnetism” *Oxford* (1961).

[6]. Callaghan, P.T. “Principles of Nuclear magnetic resonance” *Oxford* (1991).

[7]. Duer, M.J. “Solid State NMR Spectroscopy-principles and applications” *Blackwell Science LTD* (2002).

[8]. Ramsey, N.F. “Magnetic Shielding of Nuclei in Molecules” *Phys.rev*, vol 78(1950).

[9]. Fukushima, E.; Roeder, S.B.W. “Experimental pulse NMR” *Addison-Wesley Publishing Company,Inc*. (1996).

[10]. Duer, M.J. “Introduction to Solid State NMR Spectroscopy” *Blackwell Publishing* (2004).

[11]. Hahn, E.L. “Spin Echoes” *Phys.rev*, vol 80(1950).

[12]. Stejskal, E.O.; Tanner, J.E. “Spin Diffusion Measurements: Spin echoes in the presence of a time- dependant field gradient” *J.Chem.Phys*, vol 42(1964).

[13]. Tanner, J.E. “ Use of the stimulated echo in NMR diffusion studies” *J.chem.phys*, vol 52 (1969).

[14]. Meiboom, S.; Gill, D. “ Modified Spin-Echo Method for Measuring RelaxationTimes*” The review of scientific instruments*, vol 29 (1958).

[15]. Ueki, T.; Watanabe, M. “Macromolecules in ionic liquids: Progress, Challeneges and Oppertunities*” Macromolecules, The American Chemical Society* (2008).

[16]. Angewandte, *Chemie International Edition* 41, (2002).

[17]. http://u-of-o-nmr-facility.blogspot.com/2007/11/magic-angle-spinning.html

Chapter 3

^{1}H and ^{2}H NMR PFG Diffusion Studies of POLYFUEL Inc. Membranes

3.1. Introduction

Due to low operating temperature, fast start-up and easy fuel storage, direct methanol fuel cells (DMFC) are in high demand as ideal power sources for mobile applications. As the name suggests, DMFCs use liquid methanol (CH_3OH) as fuel. This choice is convenient since CH_3OH has a high specific energy density and is easily obtained from natural sources such as petroleum [1].

The most important DMFC issues are catalyst activity and membrane transport properties (i.e. desirable proton transport and undesirable water and methanol transport)[2-4]. Proton conduction may be enhanced by increasing polymer ion-exchange capacity (IEC), decreasing membrane thickness and maintaining a proper hydration level [5]. Although such strategies increase proton conduction, they often lead to increased methanol crossover. This produces excess heat and water. Overall device operation can be compromised due to resulting lower fuel efficiency and cathode activity [6].

Described in this Thesis are ^{1}H and ^{2}H NMR diffusion studies made on commercially viable sulfonated poly(arylene ether ketone) membranes produced by POLYFUEL Inc., as described in chapter 1. These results will be presented and compared with collected permeability and conductivity data.

In an NMR spectrum for liquid methanol/water, it is possible to resolve the methyl and hydroxyl protons making it feasible to measure the diffusion of the both methyl ($-CH_3$) and hydroxyl (-OH) protons separately [7-8]. However, in the case presented here, large dipolar interactions dominate the ^1H spectrum such that the $-CH_3$ and -OH proton features cannot be resolved. In order to overcome this problem, ^2H NMR measurements were done on ^2H- enriched methanol / water (CD_3OH/H_2O) solutions of varying molarities. In this way, the CD_3OH diffusing species can be studied independently of H_2O.

3.2. Experimental

3.2.1 Preparation of samples

Three Polyfuel Inc. membranes, 1.0Z, 1.2Z and 1.5Z were studied in terms of their methanol/water uptake, concentration and temperature. The polymeric samples differed in the singular aspect of IEC which was modified via the number of ion-exchange sites. Several samples were prepared and studied with different overall liquid contents and various methanol concentrations. The ratio of methanol-to-water (methanol molarity) was highest for the A-series (1.0 Z-A, 1.2 Z-A, 1.5 Z-A) at about 4M. The molarity was decreased for the B-series (1.0Z-B, 1.2 Z-B, 1.5 Z-B) and C-series (1.0Z-C, 1.2 Z-C, 1.5 Z-C) to about 2M or 3M. Membranes were cut into small pieces and then packed into 5mm NMR tubes, where the amount of membrane used for each sample was about the same. Before adding CD_3OH/H_2O, samples were completely dried inside NMR tubes under vacuum. After drying, the sample mass was recorded. First, the A-series was prepared by adding about 0.1 ml of 3M CD_3OH/H_2O solution to the respective membranes. After this, the as prepared samples were heated and maintained at 60^0 C for 16 hours. Remnant liquid was removed from the walls of the sample tube using a Kimwipe tissue. Also, if the membrane visually appeared too wet, the excess liquid was removed by exposing the sample to vacuum for a small amount of time. Following this step, the final mass of the sample was recorded in order to calculate the amount of solution uptake. Each B-series sample was prepared from its parent A-series sample by drying the parent (after measurement) under vacuum for 1-2 minutes. Correspondingly, each C-series sample was prepared by similarly drying its parent B-series sample. In this way, samples containing liquid of at least 2M could be made easily.

3.2.2 NMR studies of the membranes

NMR measurements were performed on a Varian Direct Drive spectrometer operating at 301.02 MHz for ^1H and 46.27 MHz for ^{2} H (i.e. field strength of 7.1 T). Spectroscopic references were TMS for ^1H and D_2O for ^2H. Pulse widths were about 18 μs for ^2H and 21 μs for ^1H. ^1H Self-diffusion coefficients were obtained by using a Pulse Gradient Spin-Echo (PGSE) while Pulse Gradient Stimulated Spin Echo (PGSSE) sequence was used to obtain ^2H self-diffusion coefficients as explained in chapter 2. Some typical parameters used to obtain ^1H diffusion are: $g = 1.6 – 400$ G/cm, δ and Δ equal to 2 ms and 20 ms. For ^2H diffusion, $g = 1.6 – 900$ G/cm, δ and Δ equal to 2ms and 20 ms. ^1H spin-lattice relaxation times (T_1) were evaluated from inversion recovery measurements while saturation recovery pulse sequence was used to obtained ^2H spin-lattice relaxation times as described in the chapter 2. NMR measurements were made at two temperatures, 25^0C and 50^0C.

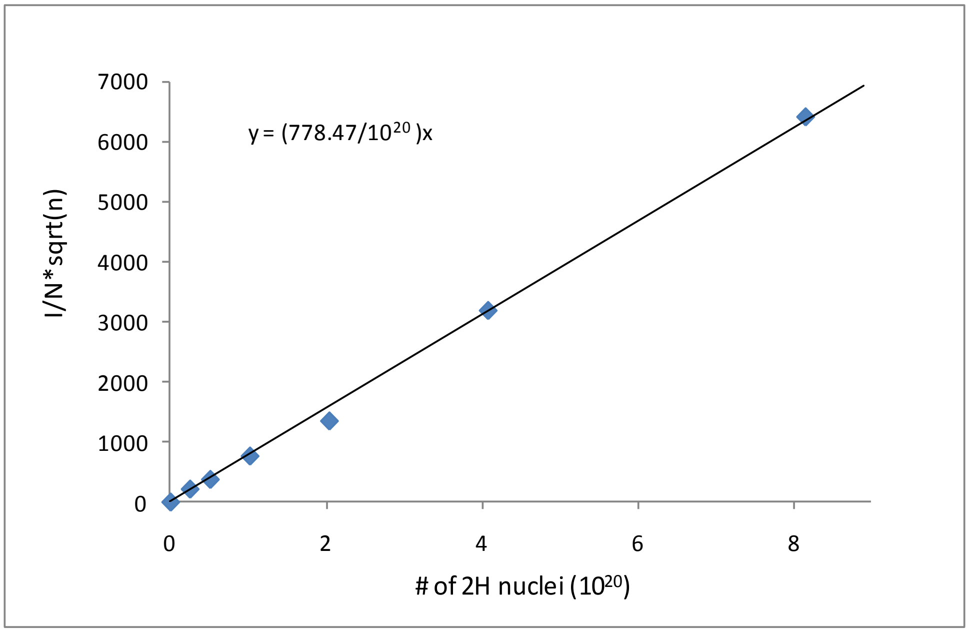

Fig 3.1: Normalized signal intensity versus # of ^{2}H nuclei

The amount of CD_3OH in the samples was determined spectroscopically as follows. Six CD3OH + H2O calibration samples were prepared with molarities of 3 M, 3/2 M, ¾ M, 3/8 M, 3/16 M, 3/32 M, and NMR spectra for each were obtained under identical conditions. A linear correlation (calibration) was found between the normalized ^{2}H NMR signal intensity and the number of ^{2}H nuclei in the sample as shown in figure 1.3. The normalized intensity is given by $(I/N\sqrt{n})$, where I is the spectrum integral, N is the root-mean-square noise factor and n is the number of acquired scans. The desired ^{2}H content is thereby found by computing the normalized intensity and using the calibration to find the corresponding number of ^{2}H nuclei. From this result, the mass and volume of water in the sample can be found by subtracting the dry sample mass along with the CD3OH mass from the sample mass. Dividing the molar amount of CD_3OH by the volume (L) of the absorbed liquid gives the molarity [9]. Table 3.1 shows the amount of methanol and water for each sample. Error of the methanol molarity is about 10%.

Sample	T(C^0)	I/(Nsqrt(n))	# of 2H (10^{20})	CD_3OH($*10^{-2}$ g)	CD_3OH ($*10^{-2}$ml)	H_2O ($*10^{-2}$ ml)	Molarity (mol/L)
1.0 Z - A	22	4252	5.46	1.06	1.34	5.17	4.6
1.0 Z - A	50	4103	5.27	1.02	1.29		
1.0 Z- B	22	1800	2.31	0.45	0.57	2.94	3.7
1.0 Z- B	50	1774	2.28	0.44	0.56		
1.0 Z - C	22	903	1.16	0.23	0.28	1.78	3.2
1.0 Z - C	50	903	1.16	0.23	0.28		
1.2 Z - A	22	3752	4.82	0.98	1.28	5.72	4.0
1.2 Z - A	50	2868	3.68	0.71	0.90		
1.2 Z - B	22	1201	1.54	0.30	0.38	4.02	1.9
1.2 Z - B	50	1129	1.45	0.28	0.36		
1.2 Z - C	22	638	0.82	0.16	0.19	2.19	1.9
1.2 Z - C	50	630	0.81	0.16	0.19		
1.5 Z - A	22	3842	4.94	0.96	1.21	5.44	4.1
1.5 Z - A	50	3561	4.57	0.89	1.12		
1.5 Z - B	22	2076	2.67	0.52	0.65	4.11	3.1
1.5 Z - B	50	1941	2.49	0.48	0.61		
1.5 Z - C	22	1909	2.45	0.47	0.61	2.26	4.7
1.5 Z - C	50	1640	2.11	0.41	0.52		

Table 3.1: Amount of methanol, amount of water and relevant molarities

3.3 Results and discussion

The figure 3.2 shows some representative spectra for the 1.0 Z membrane with various solution contents at 22 ^{0}C. Sample 1.0 Z - A has the highest amount of liquid (both methanol and water) while sample 1.0 Z – C has the lowest amount.

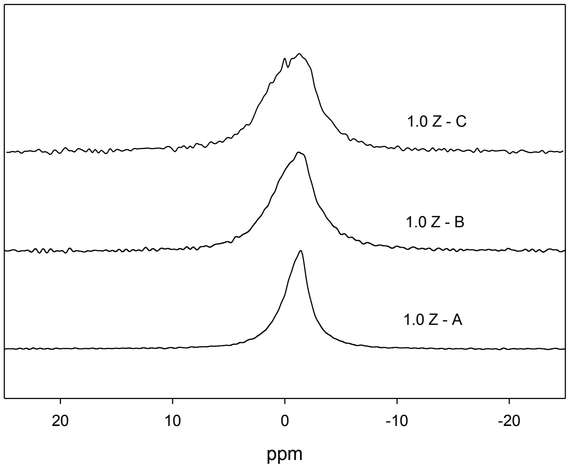

Figure 3.2: ^{2}H spectra for the 1.0 Z membrane in all three sets at 22 ^{0}C

In general, samples with smaller liquid contents give larger linewidths, as the broader resonance line is an indication of decreased motional averaging of the interactions between the nuclei and their immediate environments (i.e the host structure) [10]. The ^{2}H FWHM results are summarized in fig 3.3.

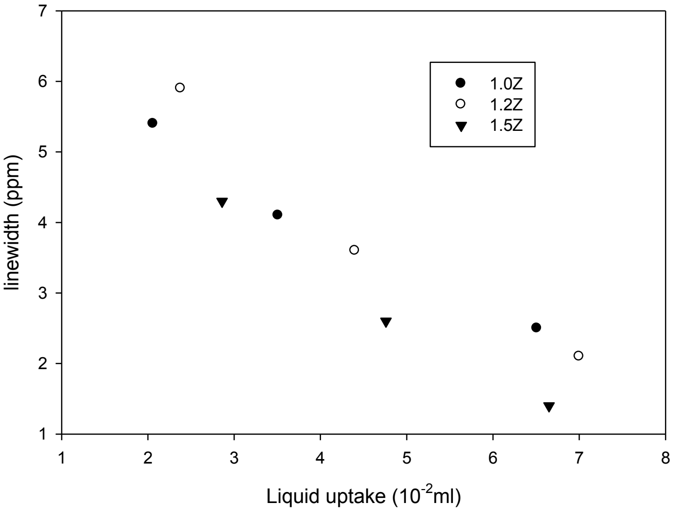

Figure 3.3: FWHM of ^{2}H spectra vs. liquid uptake at 25C for all samples

Representative ^{1}H spectra, taken at 22 ^{0}C, are shown in figure 3.4. These spectra, as revealed by the changes in linehapes, show how sensitive the membranes are to the amount of absorbed methanol and water. Clearly, the ^{1}H results are reflecting the various proton sites associated with water and the polymer itself. The spectrum peak appears around 4ppm relative to TMS, typical of H_2O.

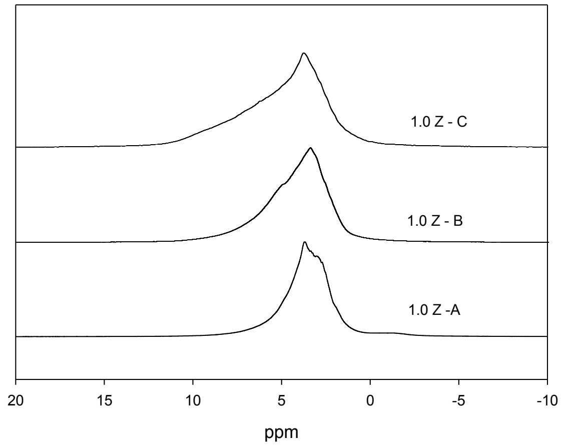

Figure 3.4: ^{1}H spectra for the 1.0 Z membrane in all three sets at 22 ^{0} C

Figure 3.5 depicts ^{1}H FWHM data for all samples at 22 ^{0}C. The results are similar to the trend found for ^{2}H. These FWHM data show that for comparable liquid contents the 1.5 Z membrane linewidths are generally lower than those of the 1.0 Z and 1.2 Z membranes. As all samples were prepared in the same manner, it can be argued that the 1.5 Z membrane absorbed more liquid (per unit amount of polymer), while the 1.0 Z membrane has the least liquid uptake.

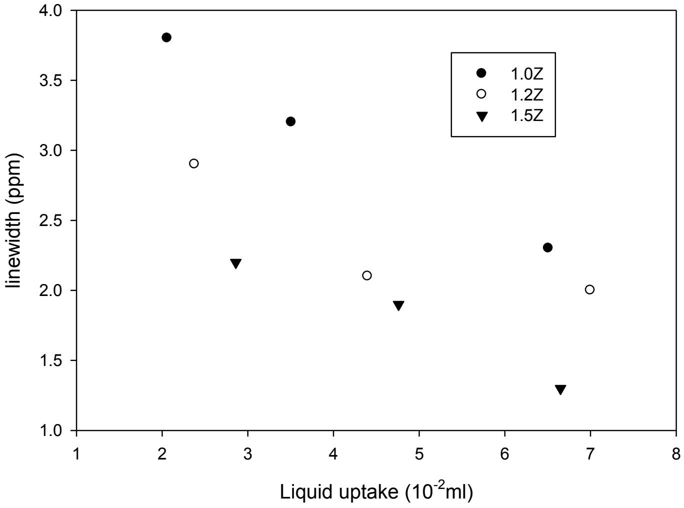

Figure 3.5: FWHM of ^{1}H spectra vs. liquid uptake at 22 ^{0}C

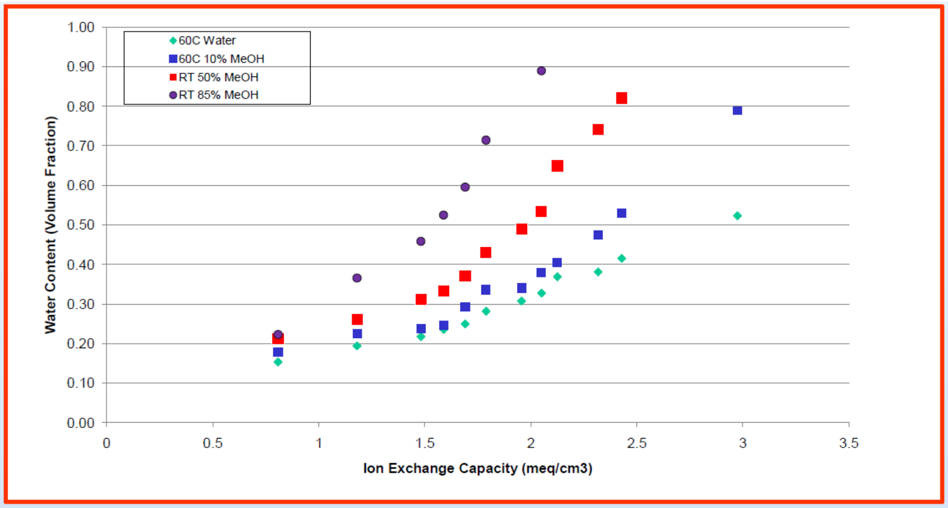

Figure 3.6: Water uptake Vs. IEC for sulfonated poly(arylene ether ketone)s.

This observation is also found in liquid uptake data versus ion exchange capacity (IEC) as measured for various liquid concentration and membranes (figure 3.6) by our Polyfuel colleagues. According to these results, liquid uptake increases with increasing IEC.

Among the membranes under consideration, 1.5 Z has the highest IEC while the 1.0Z membrane has the lowest.

Spin-lattice relaxation data for prepared samples also varies strongly with liquid content, as illustrated by the T_1 values in figure 3.7. The fact that T_1 is generally lower at the lower temperature (22^0C) and increases with the amount of liquid uptake demonstrates the liquid-like aspects of the dynamics. That is, the measurements corresponding to the "extreme narrowing limit" well above the temperature of the T_1 minimum.

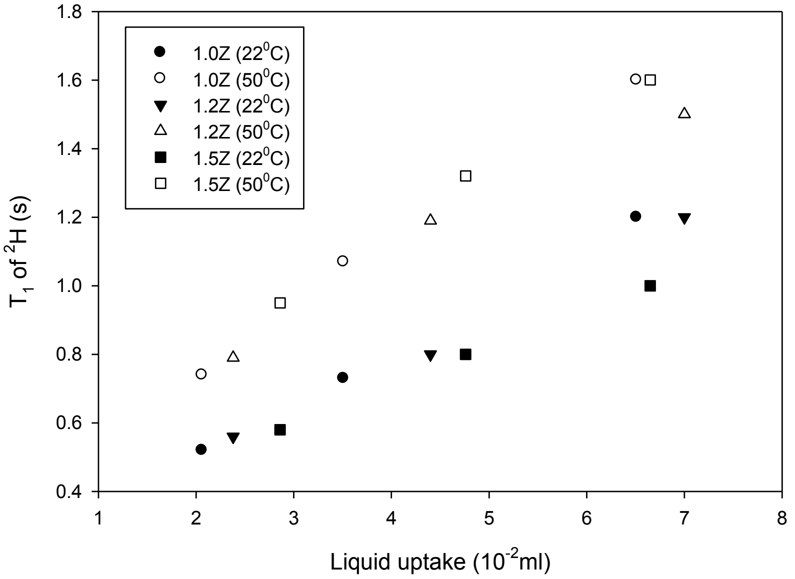

Figure 3.7: T_1 of ^{2}H vs. liquid uptake

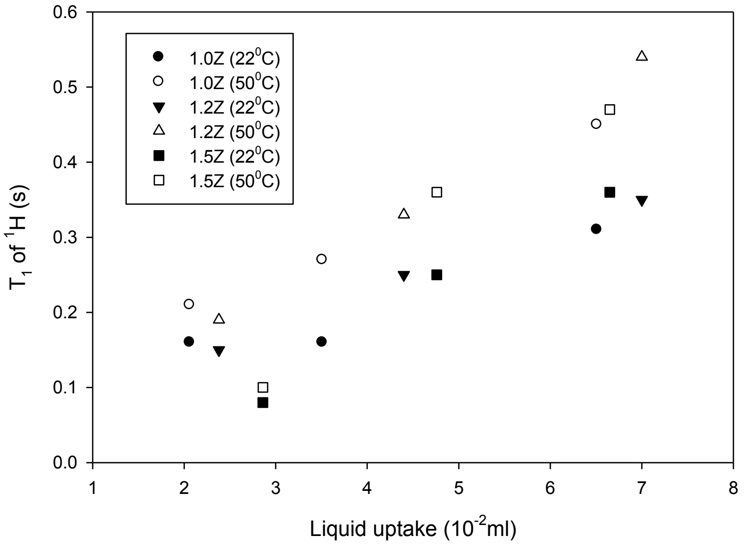

Figure 3.8: T_1 of ^{1}H vs. liquid uptake

A similar trend can be seen for ^{1}H T_1 values (figure 3.8). One important difference in the relaxation data is that the T_1 values of ^{1}H smaller than those of ^{2}H. ^{1}H is in H_2O while ^{2}H in CD_3OH. Methyl group has a rapid rotational motion compared to the motion in H_2O [11]. The other critical difference is that ^{2}H relaxes through quadrupole interactions [12]. These mentioned differences lead to the difference in T_1 values of two nuclei.

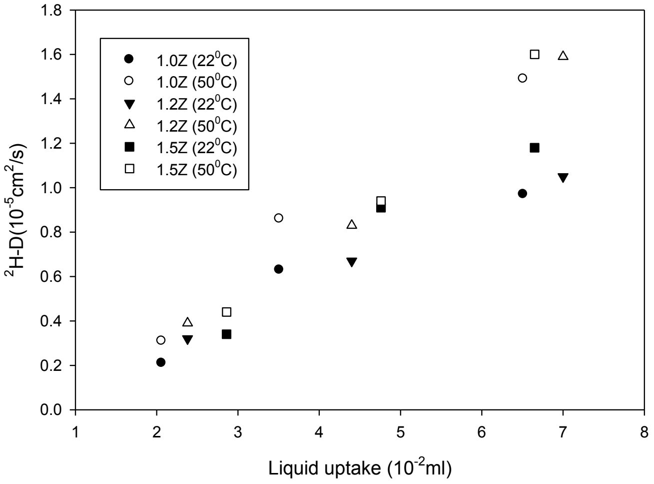

Figure 3.9: ^{2}H diffusion vs. Liquid uptake

^{2}H diffusion coefficients (figure 3.9) at 50^0C are higher than at 22^0C while diffusion coefficients increase with amount of water uptake. Figure 3.10 shows ^{1}H diffusion data at both temperatures (22 ^{0}C and 50 ^{0}C) for all samples. The similar trend as for ^{2}H diffusion can be observed for ^{1}H diffusion also.

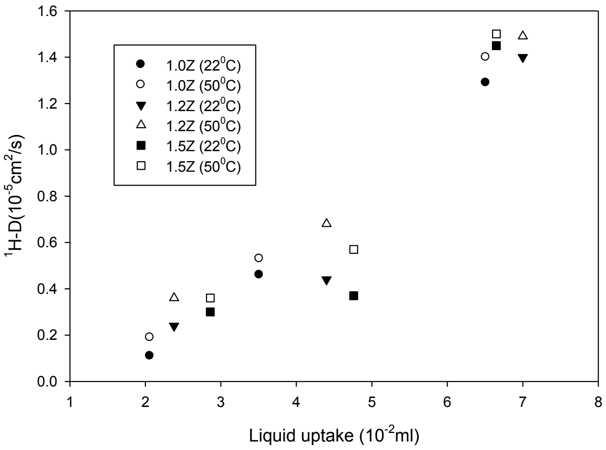

Figure 3.10: ^{1}H diffusion coefficients vs. amount of liquid uptake

In the majority of cases methanol diffusion coefficients are slightly higher than those of water. One more observation is that even if the samples 1.2 Z –B and 1.2 Z- C have the same molarities, these samples give different spin lattice relaxation values and self-diffusion coefficients; higher for wetter sample. Ratios of water to methanol diffusion coefficients are 0.92 and 0.81 for relatively dry and wet samples respectively.

Increasing ion exchange capacities (IEC) increase proton permeability and conductivity as shown in the figure 3.11. These permeability data were collected by POLYFUEL. As can be seen, 1.0 Z has the lowest permeability and conductivity.

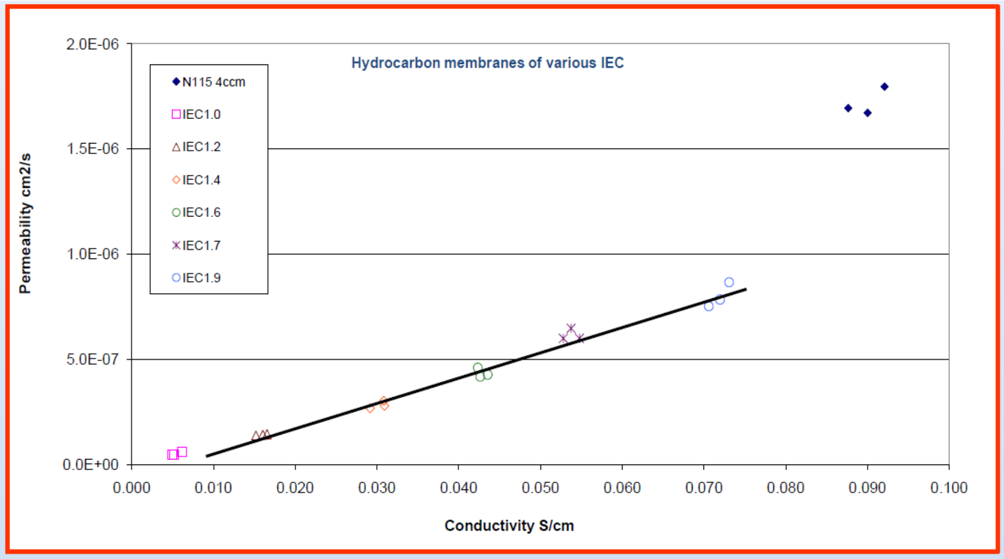

Figure 3.11: Both permeability and conductivity increase when IEC increases

Above permeability and conductivity data are supported by the NMR diffusion data for the sample series- A as shown in the figure 3.12. The sample series - A was chosen as it has comparable amount of liquid in each sample.

Both water and methanol diffusion increase with increasing IEC at both temperatures agreeing with permeability and conductivity data.

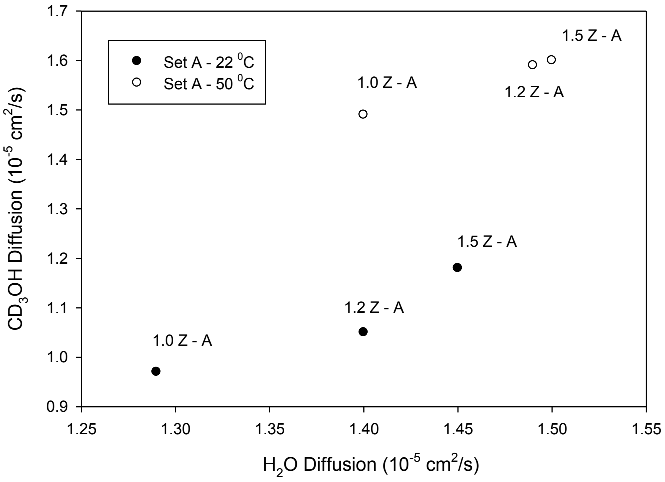

Figure 3.12: Water and methanol diffusion increase with increasing ion exchange capacity (IEC). This fact is true for permeability and conductivity also

3.4 **Summary**

Sulfonated poly(arylene ether ketone) based three polymer electrolyte membranes (1.0Z, 1.2Z and 1.5Z) have been synthesized and characterized as proton exchange membranes for direct methanol Fuel Cells (DMFC). The membranes have comparable methanol and water diffusion. Amount of liquid and the ion exchange capacity are the main factors that govern the dynamics within these membranes. Water uptake data support the NMR linewidth data. Permeability and conductivity results agree with NMR diffusion data.

References

[1]. Choi, J.; Kim, T.; Kim, S.C.; "Nafion-Sulfonated Poly(arylene ether sulfone) Composit Membrane for Direct Methanol Fuel Cell" *Macromolecular Research*. 13 (2005): 514-520

[2]. Beer, L.; Olmeijer, D.L.; Lefebcre, M.C. "Simultaneous Measurement of Proton Conductivity and Methanol Permeability for the Development of Direct Methanol Fuel Cell Membranes" *Polyfuel Inc*, Califonia.

[3]. Scott, K.; Taama, W.M.; Argyropoulos, P.; Sundmacher, K. "The impact of mass transport and methanol crossover on the direct methanol fuel cell" *J. Power Sources* 83 (1999) 204.

[4]. Every, H.A.; Hicker, M.A.; McGrath, J.E.; Zawodzinski Jr, T.A. "An NMR study of methanol diffusion in polymer electrolyte fuel cell membranes" *Journal of Membrane Science* 250(2005) 183-188.

[5]. Hickner, M.A.; Fujimoto, C.H.; Cornelius, C.J. "Transport in sulfonated poly(phenylene)s: Proton conductivity, permeability, and the state of water" *Polymer* 47 (2006) 4238–4244.

[6]. Ravikumar, M.K.; Shukla, A.K. "Effect of methanol crossover in a liquid-feed polymer-electrolyte direct methanol fuel cell" *J. Electrochem. Soc.* 143 (1996).

[7]. Nicotera, I.; Khalfan, A.; Goenaga, G.; Zhang, T.; Bocarshy, A.; Greenbaum, S. "NMR investigation of water and methanol mobility in nanocomposite fuel cell membranes" *Ionics* 14 (2008):243-253.

[8]. Jayakody, J.R.P.; Khalfan, A.; Mananga, E.S.; Greenbaum, G.S.; Dang, T.D.; Mantz, R. "NMR investigation of water and methanol transport in sulfonated polyareylenethioethersulfones for fuel cell applications" *Journal of Power Sources* 156 (2006):195-199.

[9]. www.occc.edu/kmbailey/Chem1115Tutorials/Molarity.htm, Calculating Molarity.

[10].Ye, H.; Huang, J.; Xu, J.J.; Kodiweera, N.K.A.C.; Jayakody, J.R.P.; Greenbaum, S.G. "New membranes based on ionic liquids for PEM fuel cells at elevated temperature" *Journal of Power Sources* 178 (2008):651–660.

[11]. Pavia, D.L.; Lampman, G.M.; kriz, G.S. "Introduction to spectroscopy" *Thomson Learning Inc*, third edition (2001).

[12]. Slichter, C.P. "Principle of magnetic resonance" *Happer and Row publishers* (1963).

Chapter 4

PBI – Phosphoric Acid Membranes

4.1 Introduction

Membranes used in high temperature fuel cells should not rely on the presence of water to facilitate efficient ion transport. As such, the use of traditional perfluorosulfonic acid membranes such as Nafion is severely limited. Towards the development of high temperature PEM fuel cells, membranes considered includes modified perfluorosulfonic acid, alternative sulfonated polymers, and acid-base polymer membranes [1-3]. The membranes are expected to have good thermal, chemical, and mechanical stability, in addition to high proton conductivity. In the acid-base polymer membrane category, polybenzimidazole, an amorphous basic thermoplastic is known to possess high thermal stability due to its high glass transition temperature (425 – 436^{o}C), and good chemical resistance [4]. In its natural state it is non ion-conducting. However, when doped with acids, it demonstrates an Arrhenius type ionic conductivity that depends on the acid concentration, temperature, and humidity, thus making it attractive candidate as a high temperature fuel cell electrolyte [5-6]. In addition to this, PBI is cheaper compared with Nafion, has low permeability to O_2, H_2, and CH_3OH [7]. Acids tested includes sulfuric (H_2SO_4), phosphoric (H_3PO_4), hydrochloric (HCl), perchloric ($HClO_4$), and nitric (HNO_3) [8]. It was determined that high proton conductivity could only be obtained with amphoteric acids. Of the above mentioned acids, the best dopant was found to be phosphoric acid, as it is more amphoteric than the others [9]. In addition to this, phosphoric acid has high thermal stability and low vapor pressure at elevated temperatures.

The purpose of this study was to compare the transport properties of two different kinds of PBI incorporating varying phosphoric acid concentrations. The samples were prepared by Prof. Brian C. Benicewicz of Rensselaer Polytechnic Institute (now at University of South Carolina) - Nuclear Magnetic Resonance parameters such as spin-lattice relaxation times, self-diffusion coefficients, and linewidths, were determined for both samples as a function of temperature as they are able to provide information on the mass dynamics and environments on both a short (μs) and long (ms) time range.

4.2 Experimental

In this study two PBI samples containing different monomers were investigated. The samples were phosphoric-acid doped para-PBI and dihydroxy-PBI shown in chapter 1 [10]. The phosphoric acid concentration used was 30, 50 and 70% by weight. The six different samples were investigated using NMR techniques. For NMR measurements, samples were dried at 150^{o}C in an oven for 2 and packed into 5 mm OD X 20 mm NMR tubes and sealed.

NMR measurements were performed on a Varian spectrometer and a DOTY wideline diffusion probe with ^{1}H Larmor frequencies of 301.02 MHz and a ^{31}P frequency of 121.85 MHz. Spectral information, spin lattice relaxation times (T_1) and self-diffusion coefficients (D) were obtained. Spectroscopic references were water for ^{1}H and 85% H_3PO_4 for ^{31}P. Spectral information was obtained by Fourier transforming the resulting free-induction decay (FID) of single $\pi/2$ pulse sequence. Self-diffusion coefficients were obtained by the NMR Pulse Gradient Spin-Echo technique (NMR-PGSE) as described in chapter 2. Applied gradient strengths (g) ranged from 1.5 – 900 G/cm. δ and Δ ranged from about 1.9 – 3.0 and 4 - 5 ms respectively. Spin-lattice relaxation times (T_1) were evaluated from inversion recovery measurements described in chapter 2. Variable temperature NMR measurements were made ranging from RT to 180°C, with equilibration times of 15-20 minutes following each temperature change.

4.3 Results and Discussion

4.3.1 ^{31}P analysis

^{31}P wide-line spectra are shown in Figures 4.1 and 4.2 for two temperatures, 50^0C and 150^0C, respectively for both the 2OH-PBI and para-PBI samples. At 50^oC two components are clearly observed for the 2OH-PBI samples while two and three components are observed in the para-PBI samples with increasing acid content. The chemical shifts of the peaks are ~ 0 ppm, -12 ppm, and –24 ppm respectively from left to right. The ~ 0 ppm peak is assigned to free ortho phosphoric acid as it corresponds to the reference 85% H_3PO_4 chemical shift. The ~-12 ppm and –24 ppm peaks are assigned to the pyrophosphate and tripolyphosphate groups or higher oligomers [11].

At 150^oC a single asymmetric line with chemical shift ~2 ppm is observed for the 2OH-PBI samples, the linewidth of which increases with increasing phosphoric acid (PA) content. The increased linewidth reflects greater heterogeneity of the phosphate environment, both structurally, as acid content is increased, and dynamically, as larger amplitude motions are activated at elevated temperature. The lack of component resolution further suggests rapid exchange between inequivalent phosphate sites, which has previously been recognized as a mechanism that can assist proton transport [12]. For the para-PBI samples, a single asymmetric component is also observed for the 30wt% PA content, whereas two components are resolved for the 50 and 70wt% samples, again indicating greater structural heterogeneity at higher acid content.

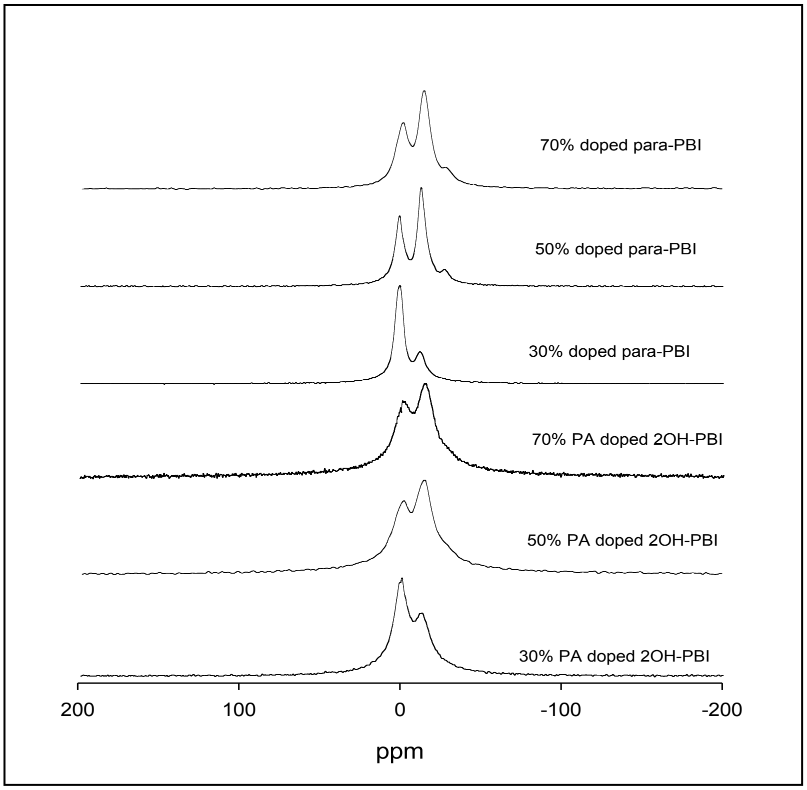

Figure 4.1: ^{31}P spectra for 2OH-PBI and para-PBI with 30, 50 and 70% phosphoric acid concentration at 50 ^{0}C.

The ^{1}H spectra at 50 ^{0}C and 150^{o}C for both the 2OH-PBI and para-PBI samples are shown in the Figures 4.3 and 4.4 respectively. At both 50 and 150^{o}C both samples displayed a main asymmetric peak centered at 6 ppm and a small peak close to 0 ppm. At 50^{o}C the linewidth of the main asymmetric peak was observed to increase with increased acid concentration for the 2OH-PBI sample.

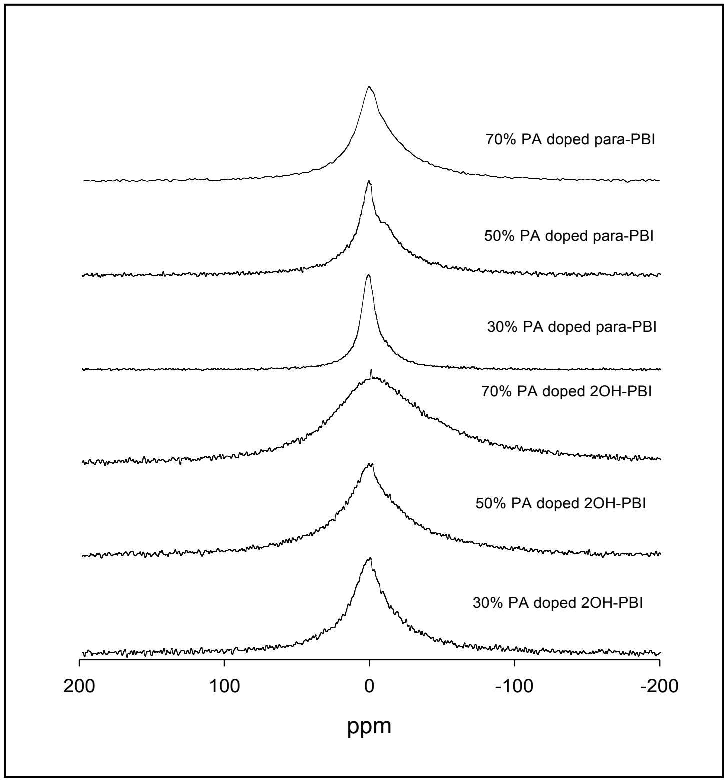

Figure 4.2: ^{31}P spectra for 2OH-PBI and para-PBI with 30, 50 and 70% phosphoric acid concentration at 150 ^{0}C.

However, the para-PBI sample showed a decrease in linewidth with increasing PA content in going from 30 to 50%, followed by a modest increase at 70%. Both samples display reduction in linewidth with increasing temperature.

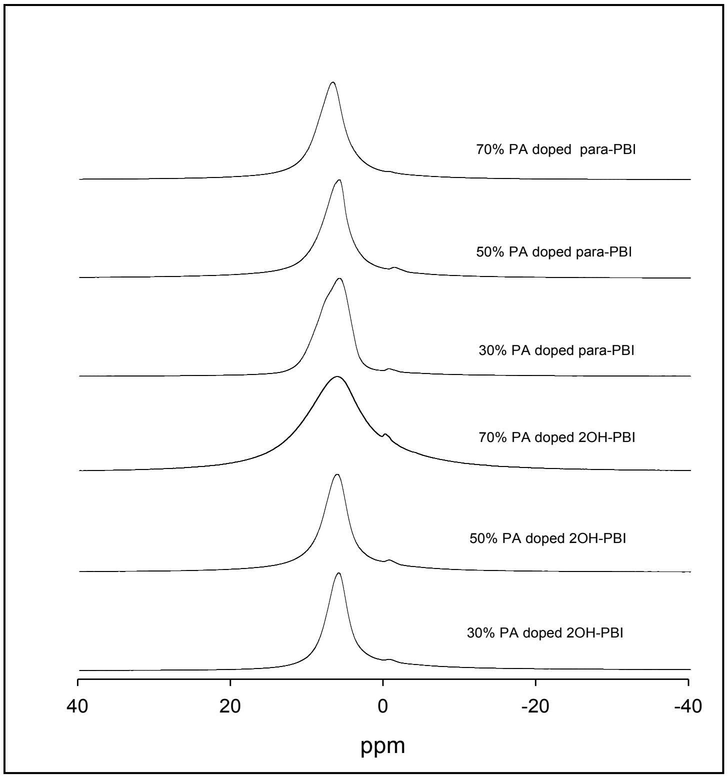

Figure 4.3: ^{1}H spectra for 2OH-PBI and para-PBI with 30, 50 and 70% phosphoric acid concentration at 50 ^{0}C.

Plotted in Figure 4.5 are ^{1}H linewidths for both 2OH-PBI and para-PBI samples as a function of temperature. The general trend in the linewidth was a decrease with increasing temperature for both samples. A decrease in linewidth is usually an indication of increased mobility (there are exceptions, an example being the previously cited ^{31}P line broadening attributed to dynamic heterogeneity at elevated temperature).

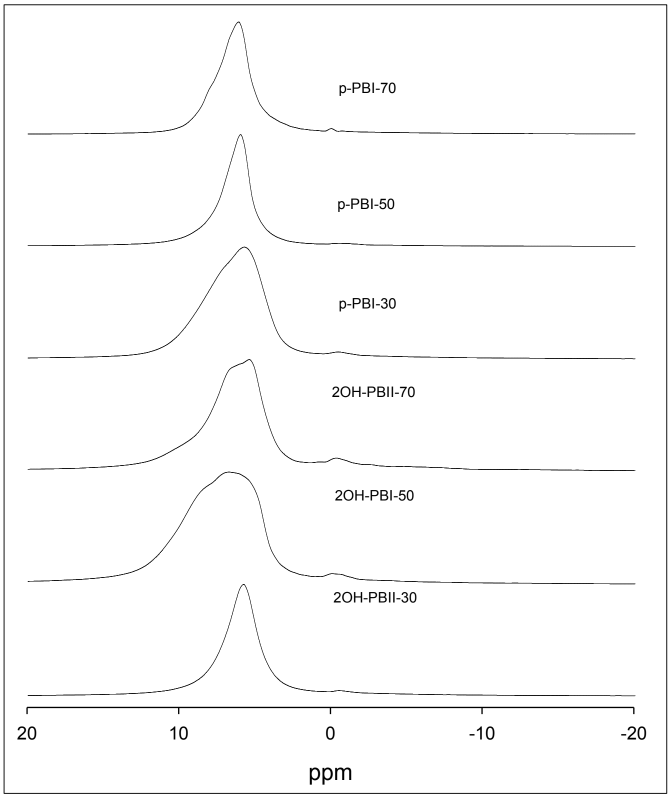

Figure 4.4: ^{1}H spectra for 2OH-PBI and para-PBI with 30, 50 and 70% phosphoric acid concentration at 150 ^{0}C.

A comparison of the two samples at equivalent PA content shows the 2OH-PBI sample having the smaller linewidth at 30% acid content. However, at both 50 and 70% PA content, that of the para-PBI sample is less. This would indicate that at 50 and 70% PA content, the protons are less restricted in the para-PBI samples compared to those in the 2OH-PBI samples.

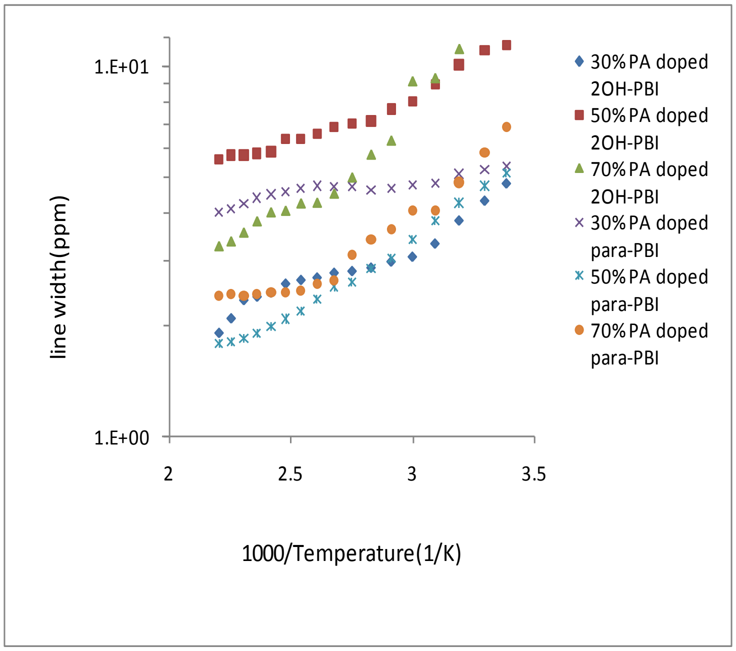

Figure 4.5: ^{1}H linewidth data for 2OH-PBI and para-PBI with 30, 50 and 70% phosphoric acid concentration as a function of temperature.

4.3.2. ^{1}H and ^{31}P T_1 data

Arrhenius plots of ^{31}P and ^{1}H T_1 data are shown in Figures 4.6 (for the 2 ppm phosphorus peak) and 4.7 respectively, for both the 2OH-PBI and para-PBI samples. The general trend was a decrease to a broad minimum or plateau with increasing temperature. For the ^{31}P nuclei the T_1 minimum occurs within the range of 383-443 K, while for the ^{1}H nuclei, it occurs between 333-393 K. The difference observed in the location of the T_1 minimum for a given sample suggests that the short-range mobility (as probed by T_1) of the phosphate and proton species is not correlated. Additionally, this also suggests that for a given PA content, the protons enjoy more mobility. For spin ½ nuclei the most dominant T_1 relaxation mechanism is dipole–dipole, which is a short-range interaction. At equivalent PA content, the 2OH-PBI sample has shorter T_1, suggesting that the short-range interactions between the PA and the PBI matrix are more dominant in this sample, therefore the mobile species are more restricted in the 2OH-PBI samples. This supports the ^{31}P spectra data which shows greater linewidth for the 2OH-PBI samples.

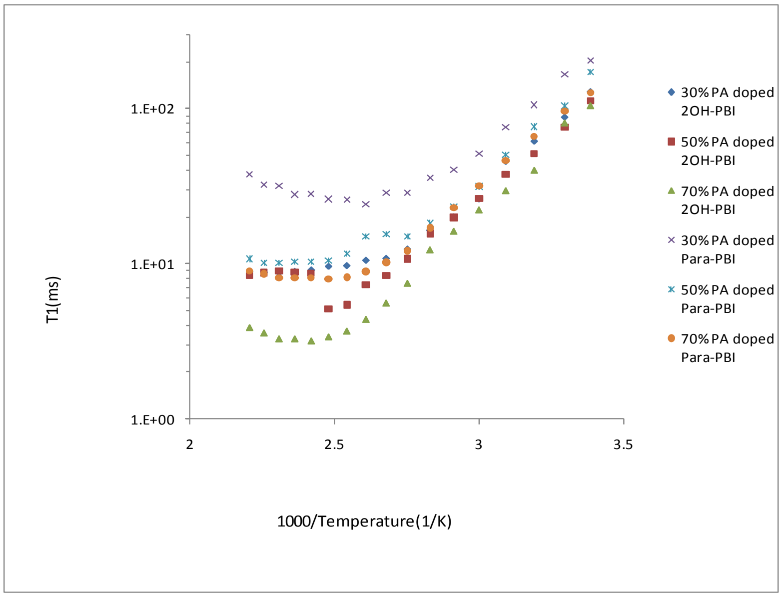

Figure 4.6: Arrhenius plots of ^{31}P T_1 data for 2OH-PBI and para-PBI (-2 ppm peak) with 30, 50 and 70% phosphoric acid concentration.

Additionally it was also observed that increasing the acid content from 30 to 50wt% resulted in an increase in the temperature at which the ^1H T_1 minimum or plateau occurred for both samples, but that further increase in acid content caused no change.

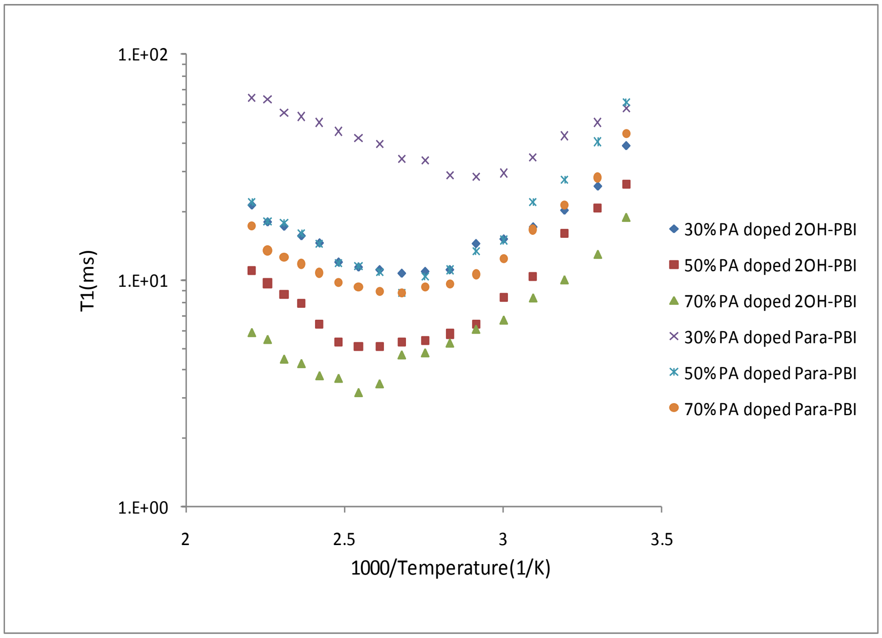

Figure 4.7: Arrhenius plots of ^{1}H T_1 data for 2OH-PBI and para-PBI with 30, 50 and 70% phosphoric acid concentration.

4.3.3. ^{1}H Self-Diffusion coefficients

^{1}H diffusion coefficients (D) data as a function of temperature for the 2OH-PBI and para-PBI samples are presented in the Figure 4.8. Due to the very short ^{31}P spin-spin relaxation times as well as short T_1's (Figure 4.6), measurements of ^{31}P D's were not possible within the limitation of reasonably attainable gradient strengths. The general trend is an increase in D with increasing temperature. For the para-PBI sample the 30% PA content sample gave the highest D values over almost the entire temperature range, with the 50 and 70% samples giving almost identical results with increasing temperature.

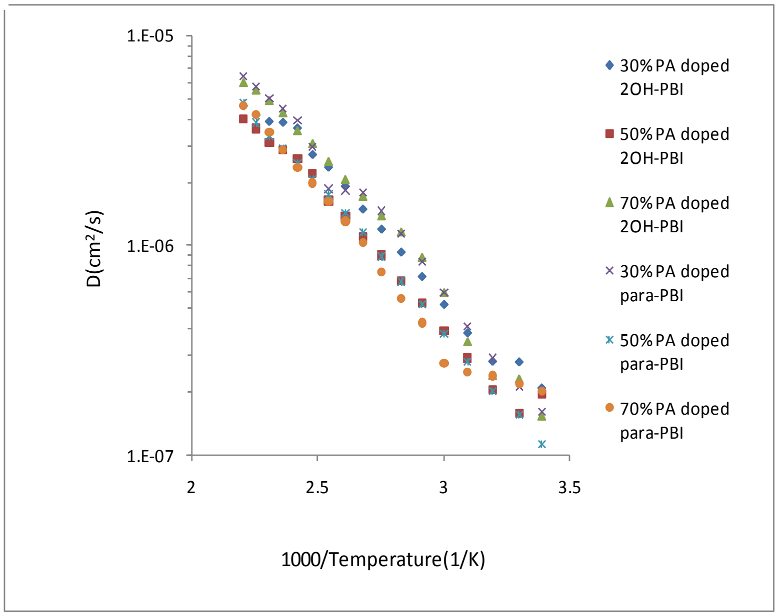

Figure 4.8: ^{1}H self-diffusion data for 2OH-PBI and para-PBI with 30, 50 and 70% phosphoric acid concentration as a function of inverse temperature.

wt% H_3PO_4	2OH-PBI (eV)	para-PBI (eV)
30	0.253	.274
50	0.258	0.27
70	0.303	0.287

Table 4.1: Calculated activation energies from the ^{1}H self-diffusion coefficient data for 2OH-PBI and para-PBI samples as a function of PA content.

For the 2OH-PBI sample the order of increasing D values is as follows in terms of PA content: 70 > 30 > 50%. A comparison of the two samples shows almost equivalent results for the 30wt% para-PBI and 70wt% 2OH-PBI samples.

Activation energies calculated from the ^{1}H D values are given in Table 4.1. While these values are consistent with that of a proton hopping mechanism [13] they increase with increasing acid content and approach the calculated value of 0.32 eV for 100% phosphoric acid [14].

4.3.4. Summary

Proton transport was characterized in two distinct PBI membranes incorporating varying concentrations of phosphoric acid. Both membranes show the presence of ortho phosphoric and pyrophosphoric acid groups, but tripolyphosphoric acid is also observed in the 50 – 70 wt% para-PBI samples. Exchange effects are observe and are conjectured to play a supporting role in the long range proton transport. The short and long range dynamics in the 2OH-PBI samples are more restricted, resulting in reduced proton transport which was increased by increasing the PA content. The effect of increasing the acid content for the para-PBI sample results in a decrease in D. This could be due to: (1) the presence of the trypolyphosphate groups, which effectively reduces the proton mass transport due to increase hydrogen bonding. This correlates with ^{1}H T_1 data which shows an increase in the T_1 minimum temperature with increasing PA content. This effect is also observed in the 2OH-PBI sample, except no monotonic trend is observed for D. This could be a result of differences in the samples caused by their different preparation methods. Activation energies obtained from the ^{1}H D data supports a proton hopping mechanism, with assistance from fast phosphorus nuclei exchange between the various phosphate groups. However, with increasing acid content the value approaches that observed in 100% PA – a system with significant hydrogen bonding and one whose ionic conductivity is due almost entirely to proton transport.

References

[1]. Li, Q.; He, R.; Jensen, J.O.; Savinell, R.; Bjerrum, N. *Progress in Polymer Sci*. **2009**, 34, 449.

[2]. Li, Q.; He, R.; Jensen, J.O.; Bjerrum, N. *Chemistry of Mater*. **2003**, 15(26), 4896.

[3]. Santiago, E.I.; Isidoro, R.A.; Dresch, M.A.; Matos, B.R.; Linardi, M.; Fonseca, F.C. *Electrochim. Acta*. **2009**, 54, 4111.

[4]. Chung, T.S. *J. Macromol. Sci*. **1997**, C37, 277.

[5]. Bouchet, R.; Siebert, E. *Solid State Ionics*, **1999**, 118, 287.

[6]. Fontanella, J.J.; Wintersgill, M.C.; Wainright, J.S.; Savinell, R.F.; Litt, M. *Electrochim. Acta*, **1998**, 43, 1289.

[7]. Kongstein, D.E.; Berning, T.; Borresen, B.; Seland, F.; Tunold, R. *Energy*, **2007**, 32, 418.

[8]. Xing, B.; Savadogo, O. *J. New Mater. Electrochem. Systems*, **1999**, 2, 95.

[9]. Lassegues, J.C. Mixed Inorganic-Organic systems: *the acid/polymer blends. In: Colomban Ph, editor. Proton conductors, solids, membranes and gels-materials and devices.* Cambridge Univ. Press, **1992**, p. 311.

[10]. Xiao, L.; Zhang, H.; Scanlon, E.; Ramanathan, L.S.; Chloe, E-W.; Rogers, D.; Apple, T.; Benicewicz, B.C. *Chem. Mater*. **2005**, 17, 5328.

[11]. Crutchfield, M.M; Callis, C.F.; Irani, R.R.; Roth, G.C.; *Inorg. Chem*., **1962**, 1, 813.

[12]. Jayakody,J.R.P.; Chung, S.H.; Durantino, L.; Zhang, H.; Xiao, L.; Benicewicz, B.C.; and Greenbaum, S.G., J. Electrochem. Soc. **2007**, 154, B242.

[13]. Chandra, S, *Proceedings of the II International Symposium on Solid State Devices*, Chowdari, B.V.; Radakrishna, S.; Editors. World Scientific Publication, Singapore, **1988**.

[14]. Dippel, T.; Kreuer, K.D.; Lassegues, J.C.; Rodriguez, D. *Solid State Ionics*, **1993**, 61, 41.

Chapter 5

PBI - Ionic Liquid Membranes

5.1. Introduction

This work aims to demonstrate the feasibility of the concept of [acid/ionic liquid/polymer] composite gel-type proton conducting membranes that can serve as practical membranes for operation of PEM fuel cells at 150 °C. PBI possesses excellent thermal and chemical stability as well as its base property which makes it easy to interact with acid components, so that PBI is more suitable to apply to high temperature membranes. In this chapter, investigation of novel H_3PO_4/$PMIH_2PO_4$/PBI composite membranes (chapter 1) is presented to suggest their feasibility for PEM fuel cell operated at elevated temperature. The NMR results of the publication "New membranes based on ionic liquid for PEM fuel cells at elevated temperatures" by H. Ye, J.Huang, J.J Xu, N.K.A.C Kodiweera, J.R.P Jayakody and S.G Greenbaum are described here.

5.2. Experimental

For NMR measurements, samples were dried at 150 °C in a vacuum oven for 2 h and packed into 5mm NMR tubes and flamed-sealed. NMR measurements were performed on a Chemagnetics CMX-300 spectrometer with ^1H Larmor frequencies of 301.02MHz and a ^{31}P frequency of 121.85 MHz. Spectroscopic references were distilled water for ^1H and 85% H_3PO_4 for ^{31}P. Spectral information was obtained by Fourier transforming the resulting free-induction decay (FID) of single $\pi/2$ pulse sequence. Pulse widths were about 5μs for ^{31}P and 12μs for ^{1}H. Self-diffusion coefficients (D) were obtained by the NMR pulse gradient spin–echo technique as explained in chapter 2. Applied gradient strengths (g) ranged from 2 to 220 G/cm, δ and Δ ranged from about 1 to 5 and 5 to 20 ms respectively. Uncertainties in self-diffusion coefficient values are ~5%. Spin–lattice relaxation times (T_1) and spin-spin relaxation times (T_2) were evaluated from techniques as explained in chapter 2. Variable temperature NMR measurements were made ranging from ambient to 180 ◦C, with equilibration times of 20–25 min following each temperature change.

5.3. Results and discussion

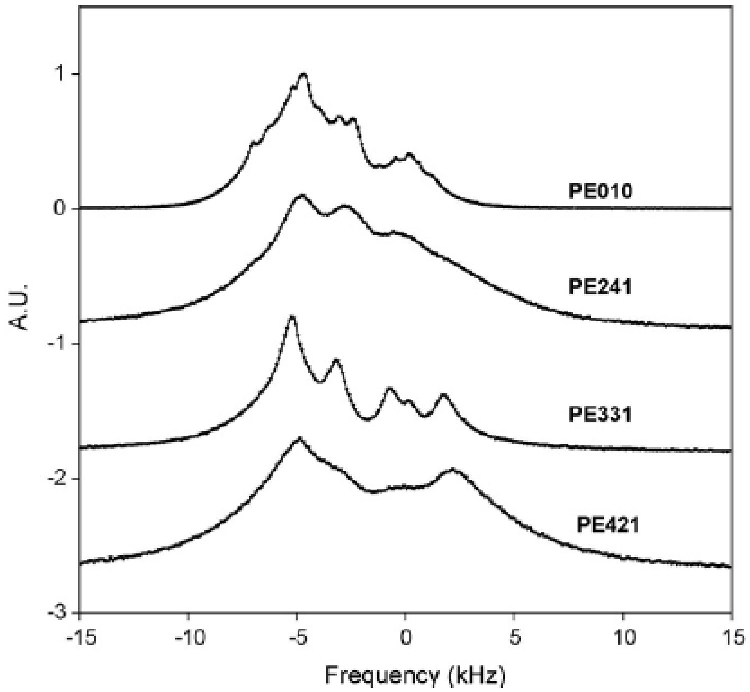

Figure 5.1: ^{1}H spectra of reference ionic liquid and membranes at 295K, where the numbers xyz are the mole ratios of H_3PO_4, ionic liquid and PBI respectively.

Fig. 5.1 displays ^{1}H spectra for four different ratios of H_3PO_4/$PMIH_2PO_4$/PBI. The spectrum 0/1/0 is for the pure ionic liquid ($PMIH_2PO_4$) shown for reference purposes. A detailed spectral assignment will not be given here, as the main purpose is to identify the dynamics of the various mobile species. Briefly, the largest feature (including the "shoulder") of the ionic liquid spectrum centered around ~4.8 kHz from the reference frequency is assigned to the *N*-propyl and *N*-methyl protons, the peak roughly in the middle (around −3 kHz from the reference) is assigned to imidazole ring protons and the feature around 0 kHz is attributed to POH protons of the $H_2PO_4^-$ anion. The assignments of the membrane NMR spectra can thus be made, assuming that the rigid PBI protons contribute no more than a broad baseline to the spectrum, on the basis of what happens when H_3PO_4 is added. Clearly, the addition of H_3PO_4 gives a spectral contribution +2 kHz from the reference. In this manner, monitoring the relaxation recoveries and diffusive decays of the *N*-alkyl protons and the H_3PO_4 will permit dynamical analysis of the IL cation and acid protons, the latter being of more direct relevance to membrane performance in a fuel cell. This argument does not yet take into account the effect of exchange between the protons of the IL anion and the H_3PO_4, which will be addressed later.

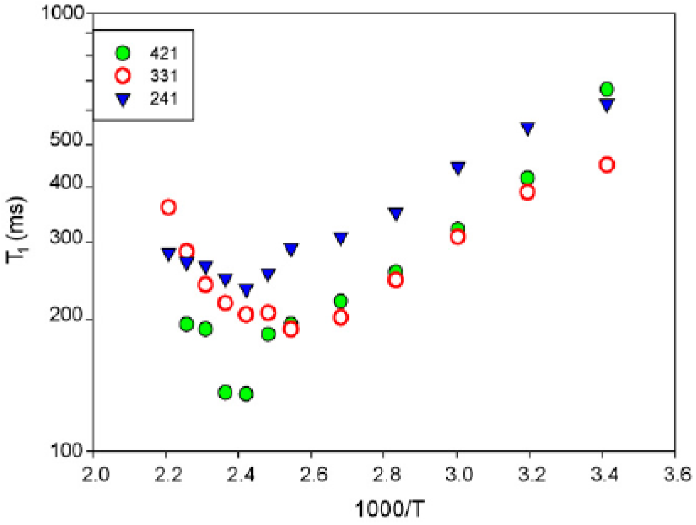

Figure 5.2: NMR ^{1}H T_1 relaxation results for IL site of H_3PO_4/$PMIH_2PO_4$/PBI membranes.

Arrhenius plots of ^{1}H T_1 of PMI and H_3PO_4 for H_3PO_4/$PMIH_2PO_4$/PBI membrane samples are displayed in Figures 5.2 and 5.3, respectively. All mobile species exhibit T_1 minima between 125 and 145 ◦C. A T_1 minimum occurs when the motional correlation time is comparable to the reciprocal of the Larmor angular frequency (in the present case, around 10^{-9} s) [1]. Thus it can be concluded that on the whole, all mobile species are dynamically correlated, which in turn suggests that the H_3PO_4 is well mixed with the ionic liquid phase on the nanoscale. In addition to short range translational motion, methyl group rotation can also provide an efficient relaxation mechanism. However there are subtle differences between the relaxation behaviors of the different proton sites in a given compound and between proton sites among the various membranes. In particular, local motion of the *N*-alkyl protons in the 3/3/1 membrane is enhanced as evidenced by its lower temperature T_1 minimum, which is consistent with smaller linewidths of individual components of this compound (Fig. 5.1). On the other hand, the POH protons in the 3/3/1 membrane exhibit a higher temperature T_1 minimum. The short range motions responsible for relaxation likely includes H^+ hopping between POH sites.

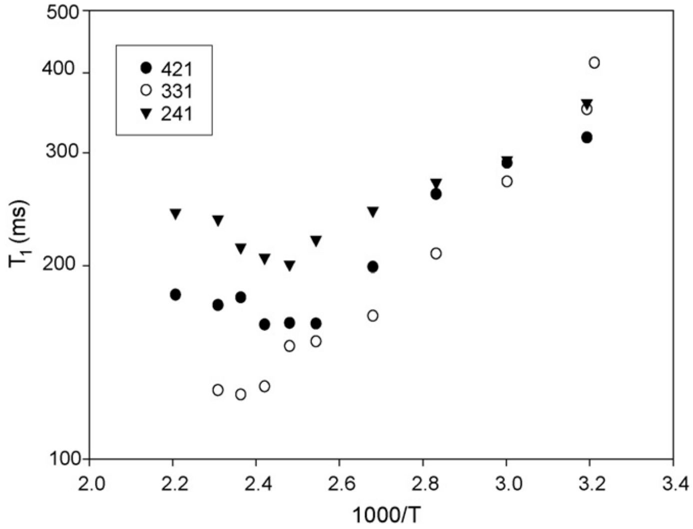

Figure 5.3: NMR ^1H T_1 relaxation results for phosphate-associated protons in $H_3PO_4/PMIH_2PO_4/PBI$ membranes.

^{31}P spectra at 100 °C of $H_3PO_4/PMIH_2PO_4/PBI$ membranes are shown in figure 5.4. All three spectra exhibit two main peaks with a relatively narrow component at the reference frequency indicating some amount of free H_3PO_4 and the broad peak is attributed to the short range intermixing of H_3PO_4 with PBI and the IL. T_2 values of three different membranes were measured and they are short, about 1–2 ms over the temperature range of 20–180 °C. The broad line width and short T_2, even at high temperature, is attributed to the greater restriction of both translational and rotational phosphate group motion by the strong interaction with the host structure.

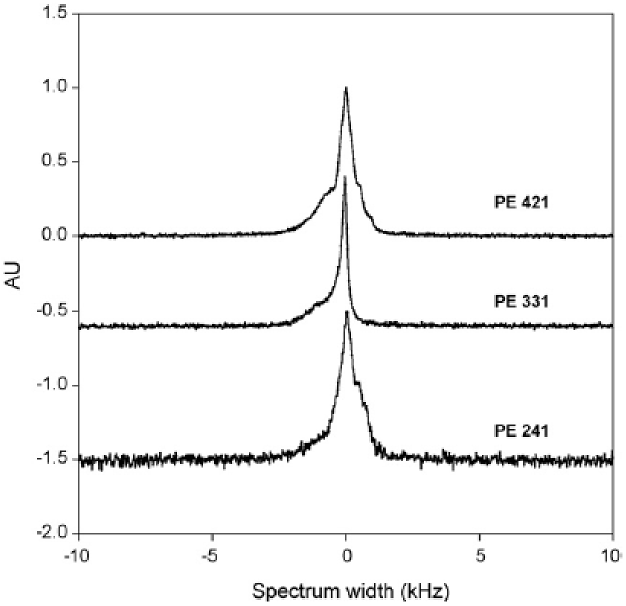

Figure 5.4: ^{31}P NMR spectra of $H_3PO_4/PMIH_2PO_4/PBI$ membranes.

Arrhenius plots of ^{31}P T_1 for $H_3PO_4/PMIH_2PO_4/PBI$ samples are displayed in figure 5.5 and it is clear that the spin–lattice relaxation is quite similar among the materials, an indication of the close similarity of the local environment of the phosphate ions in all samples. A T_1 minimum is observed in the 2/4/1 membrane and is believed to occur above the temperature range of this investigation for the other two compounds. Low T_1 values at higher temperature also contribute to the ^{31}P linewidth *via* lifetime broadening.

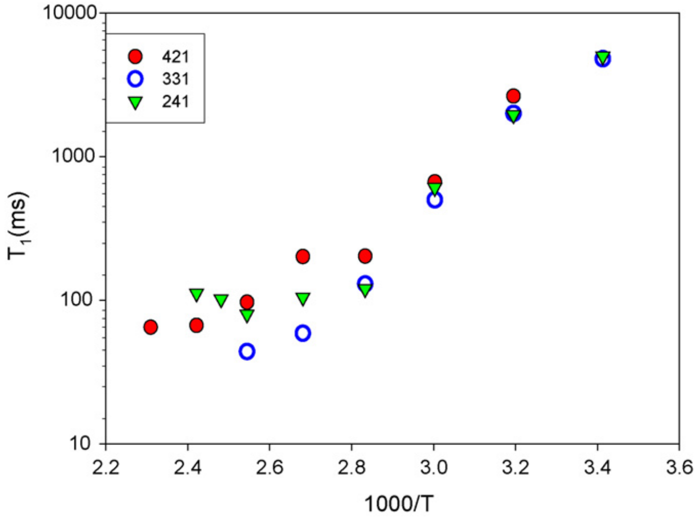

Figure 5.5: NMR ^{31}P T_1 relaxation results for the acid site of H_3PO_4/PMIH_2PO_4/PBI membranes.

Proton diffusion results for H_3PO_4/PMIH_2PO_4/PBI samples, extending to 180 ˚C are displayed in figure 5.6. The values are presented for two main peaks, corresponding to the *N*-alkyl protons and the POH protons. As expected, the diffusion coefficients increase with increasing temperature. The diffusion values of POH are higher than those of IL cation for all three samples, with the largest difference occurring for PE241. Previous studies of pure H_3PO_4 and H_3PO_4 in water have shown that the phosphate ions diffuse through a vehicular mechanism that depends on the solution viscosity, whereas acid protons diffuse *via* a hopping mechanism that is uncorrelated with viscosity [2]. In the present case, it is surmised that the IL cationic motion is vehicular while the acid protons also have a hopping pathway available. This may include rapid exchange between protons in the H_3PO_4 and the IL anion. The lack of clear resolution between the POH from the ionic liquid and the POH from the phosphoric acid (Figure 5.1) is consistent with proton exchange between these species, not unlike what has been observed in other phosphoric acid/PBI membranes where more than one phosphate species is present [3].

Although the diffusion coefficients have the highest value for the membrane with the highest ionic liquid concentration (PE241), the next highest values occur for the membrane with the lowest IL concentration (PE421). It is interesting that the intermediate IL concentration membrane (PE331) gives the smallest difference between diffusion values of IL cation and acid protons, suggesting strong interactions among all components.

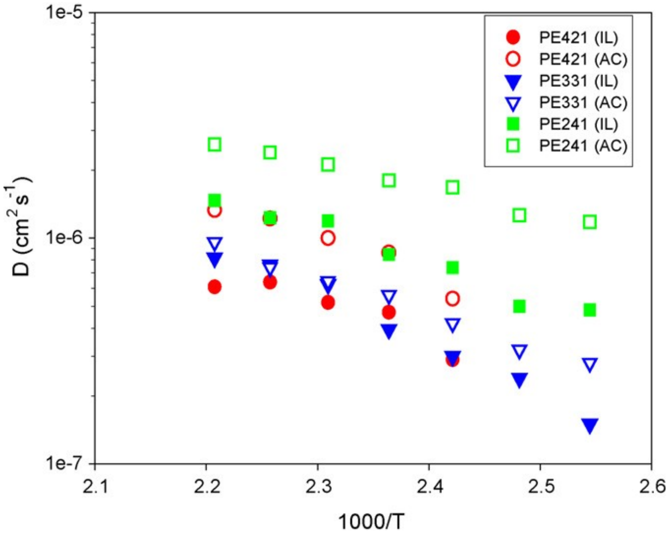

Figure 5.6: Temperature dependence of the proton diffusion in H_3PO_4/$PMIH_2PO_4$/PBI membranes.

It was not possible to measure the ^{31}P diffusion coefficient of the membranes due to the short T_2 (1–1.5 ms) values, over entire temperature range. Given the highest value of T_2 ≈2.0 ms observed for the membrane, which occurred at high temperature, and experimental limitations on gradient strengths, it is possible to estimate an upper limit of D that is consistent with the lack of observable echo decay, and that value is about 10^{-8}

cm^2 s^{-1}. Thus there is negligible phosphate diffusion in these materials; i.e. about two orders of magnitude lower than the proton diffusion coefficients.

The ionic liquid will disperse homogeneously into the H_3PO_4/PBI complex due to its having the same anion as H_3PO_4. Combined with the good thermal and chemical stability of PMI^+ cation, it is reasonable to conclude that incorporating $PMIH_2PO_4$ will not compromise the advantages of H_3PO_4-doped PBI membranes such as good proton conductivity, zero electro-osmotic water drag number, low gas permeability, and excellent oxidative and thermal stability [4–14]. Moreover, it is expected that there would be a three-dimensional hydrogen bonding network (figure 5.8) within the H_3PO_4/$PMIH_2PO_4$/PBI membranes and proton conduction would occur mainly through the hydrogen bonding network by a hopping mechanism.

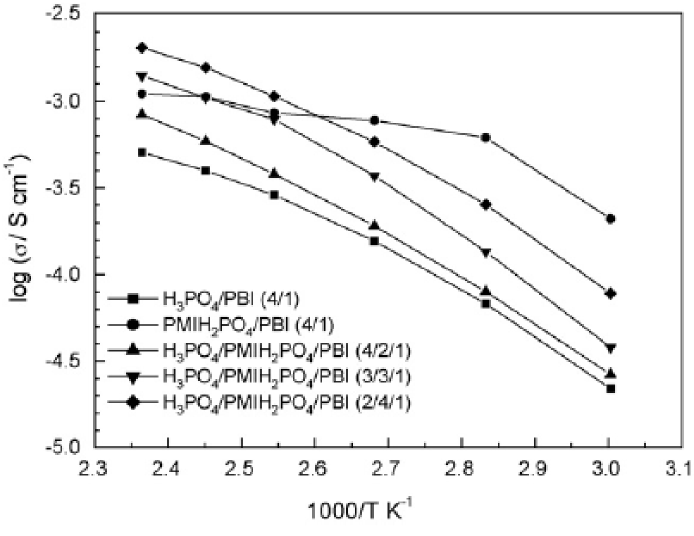

Figure 5.7: Temperature dependent ionic conductivity of H3PO4/PBI, PMIH2PO4/PBI and H3PO4/PMIH2PO4/PBI membranes under anhydrous [17].

Figure 5.7 displays the Arrhenius plot of ionic conductivity obtained by our collaboration at Rutgers University; of H_3PO_4/PBI, $PMIH_2PO_4$/PBI and H_3PO_4/$PMIH_2PO_4$/PBI membranes with different component molar ratio. H_3PO_4/PBI and H_3PO_4/$PMIH_2PO_4$/PBI membranes exhibit similar temperature dependent conductivity and following VTF behavior [15–17], which indicates these membranes have similar ionic conduction mechanisms. However, the conductivity of $PMIH_2PO_4$/PBI membrane has weaker temperature dependence at temperature higher than 80 °C. In this particular sample there is probably a negligible proton contribution to the total ionic conductivity. Incorporating ionic liquid into H_3PO_4/PBI complex significantly increases the ionic conductivity of the membranes; a higher content of $PMIH_2PO_4$ yields a higher ionic conductivity for the membrane. Under completely anhydrous conditions, these H_3PO_4/$PMIH_2PO_4$/PBI membranes with 4/2/1, 3/3/1, and 2/4/1 compositions exhibit conductivities 0.84, 1.40 and 2.04 mS cm^{-1} at 150 °C, respectively. The 2/4/1 material also has the highest POH proton diffusivity.

In the H_3PO_4/$PMIH_2PO_4$/PBI membrane, though there are several mobile ions including PMI^+ cation and $H_2PO_4^-$ anion, only proton transport is relevant for fuel cell power production, other two will only induce the polarization of the fuel cell. The ^1H NMR diffusion results suggest that proton transport is the main contribution to the total ionic conductivity of the membranes. Tests in fuel cells and other analysis are yet to be carried out to evaluate these materials further. Of course, whether the thermal, mechanical and chemical stability of H_3PO_4/$PMIH_2PO_4$/PBI membranes is sufficient to maintain a satisfactory performance after long-term operation still needs to be established.

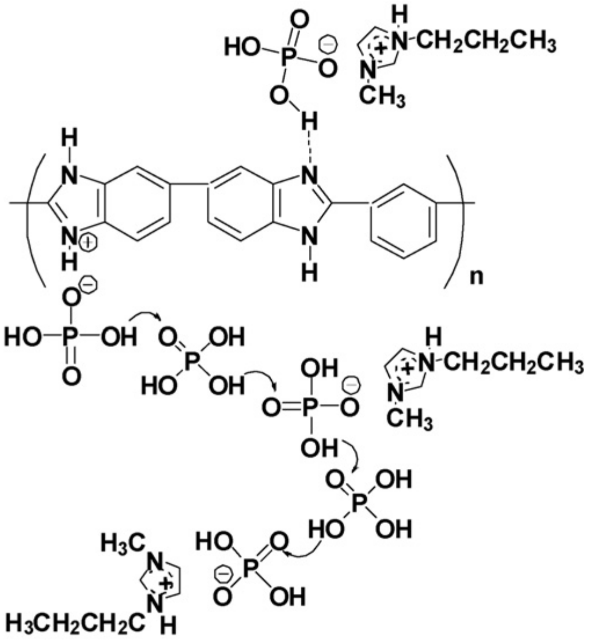

Figure 5.8: Proton hopping pathways

5.4. **Summary**

[Acid/ionic liquid/polymer] polymer gel electrolyte membranes have been synthesized and characterized as prospective proton exchange membranes for PEM fuel cells operating at elevated temperature. Novel H_3PO_4/PMIH_2PO_4/PBI composite gel-type proton conducting membranes have been prepared using lab synthesized thermal engineering polymer polybenzimidazole (PBI) and ionic liquid, PMIH2PO4, with the proton accepting anion $H_2PO_4^-$. The membranes have acceptable ionic conductivity of up to 2.0×10^{-3} S cm^{-1} at 150 ◦C and under anhydrous condition. NMR self-diffusion for the POH protons and conductivity data are consistent with the PE 241 membrane showing the highest values. H_3PO_4/PMIH_2PO_4/PBI membranes combine the advantage of H_3PO_4-doped PBI and special features of ionic liquid PMIH_2PO_4. A three-dimensional hydrogen bonding network structure in the H_3PO_4/$PMIH_2PO_4$/PBI membranes is proposed and proton conduction occurs mainly through the hydrogen bonding network by a hopping mechanism. The ionic liquid $PMIH_2PO_4$ is surmised to function as proton transfer bridges, a plasticizer for PBI, a balancer of the strengths of hydrogen bonding in the system, and an absorber and retainer of water.

References

[1]. Abragam, A. “Principles of Nuclear Magnetism” *Oxford University Press* 1961.

[2]. Chuang, S.H.; Bajue, S.; Greenbaum, S.G. *J. Chem. Phys*. 112 (2000) 8515.

[3]. Jayakody, J.R.P. *et al., J. Electrochem. Soc*. 154 (2007) B242.

[4]. Wainright, J.S.; Wang, J.; Weng, D.; Savinell, R.F.; Litt, M. J. *Electrochem.Soc*. 142 (1995) L121.

[5]. Samms, S.M.; Wasmu, S.; Savinell, R.F. *J. Electrochem. Soc*. 143 (1996)1225.

[6]. Wang, J.T.; Savinell, R.F.; Wainright, J.; Litt, M.; Yu, H. *Electrochim. Acta* 41 (1996) 193.

[6]. Wang, J.T.; Wainright, J.; Savinell, R.F.; Litt, M. *J. Appl. Electrochem*. 26 (1996) 751.

[7]. Weng, D.; Wainright, J.S.; Landau, D.; Savinell, R.F. *J. Electrochem. Soc*.143 (1996) 1260.

[8]. Fontanella, J.J.; Wintersgill, M.C.; Wainright, J.C.; Savinell, R.C.; Litt, M. *Electrochim. Acta*. 43 (1998) 1289.

[9]. Bouchet, R. *E. Siebert, Solid State Ionics* 118 (1999) 287.

[10]. Glipa, X.; Bonnet, B.; Mula, B.; Jones, D.J.; Roziere, J.; Mater. *J.Chem*. 9 (1999) 3045.

[11]. Xing, B.; Savadogo, O.*;* *J. New Mater. Electrochem. Syst*. 2 (1999) 95.

[12]. Li, Q.; Hjuler, H.A.; Bjerrum, N.J.; *J. Appl. Electrochem*. 31 (2001) 773.

[13]. Kawahara, M.; Morita, J.; Rikukawa, M.; Sanui, K.; Ogata, N. *Electrochim. Acta* 45 (2002) 1395.

[14]. Vogel, H. *Phys. Z.* 22 (1921) 645.

[15]. Tamman, G.; Hesse, W.; Aborg. Z. *Allg. Chem*. 156 (1926) 245.

[16]. Fulcher, G.S. *J. Am. Ceram*. Soc. 8 (1925) 339.

[17]. Ye, H.; Huang, J.; Xu, J.J.; Kodiweera, N.K.A.C.; Jayakody, J.R.P.; Greenbaum, S.G. *Journal of power sources* 178 (2008) 651-660.

Chapter 6

Activated Carbon Study

6.1. Introduction

The objective of this study is to investigate the role of phosphorus and its compounds on the electrochemical performance of activated carbons. Although phosphorus is not a commonly encountered element in activated carbon it is always present in measurable quantity in carbons obtained using phosphoric acid activation [1, 2].

In this study the chemical environment of phosphorus is investigated in conjunction with oxygen and nitrogen functional groups. In that light, the speciation of nitrogen and oxygen containing groups is revisited and an attempt is made to elucidate the effect of phosphorus on the measured capacitance and capacitance retention ratio. This study reveals how the phosphorus incorporated into the carbon matrix affects the performance of carbon electrodes. This chapter originates from the publication “Effect of surface phosphorus functionalities of activated carbon containing oxygen and nitrogen on electrochemical capacitance” and for the most part, only the NMR results are described in detail.

6.2. Experimental

The samples (BAX, BAX-O, BAX-U, BAX-UO, BAX-M, BAX-MO) as mentioned in chapter 1 were studied using ^{31}P magic-angle spinning nuclear magnetic resonance (MAS NMR) spectroscopy as described in chapter 2. Measurements were performed on a Varian-S spectrometer operating at 122 MHz (^{31}P Larmor frequency) and spinning speed of 22 kHz. NMR-ready samples were prepared under ambient lab conditions by packing as-given or minimally ground powders into 3.2mm thick wall rotors. Pulse width was 3.25 μs while recycle delay was 1 s. Depending on the sample, 12 k to 60 k FIDs were signal averaged before processing. The spectral frequency scale, as given in the normalized units of ppm, is relative to the ^{31}P chemical shift of 85% H3PO4.

6.3. Results and discussion

NMR Analysis

^{31}P MAS NMR spectra are shown in Fig. 6.1. The only interaction represented in the spectra is that due to chemical shift isotropy (all other relevant interactions are ‘‘averaged out’’ from MAS); therefore, the line shapes strictly demonstrate the phosphorous site heterogeneity within each sample. The ^{31}P spectra can be generally described in terms of two features: a narrow component and a broad component, which can be separated via simulation. As is often the case for MAS lineshapes, it is found that the narrow features are best simulated using Lorentzian–Gaussian convolution (Voight) lineshapes,

$$\Gamma(x) = \frac{A}{\sigma\sqrt{\pi}} \int_{-\infty}^{\infty} \frac{\exp\left(-f^2\right)}{\left(\zeta^2 + \left(\frac{x-\delta_{iso}}{\sigma} - f\right)^2\right)} df \qquad (6.1)$$

where f is the integration variable, A is the amplitude, σ is a width parameter, ζ is a parameter related to the ratio of widths of Lorentzian to Gaussian and δ_{iso} is the isotropic shift or center-of gravity (cog). The amount of Lorentzian character increases with the parameter *f*. It could be seen that for the value of $f = 0.54$ provides a mostly Gaussian shaped peak along with a broad Lorentzian style base. The broad component, which is not well simulated by $\Gamma(x)$, can be isolated through subtraction of the weighted narrow component simulation from the total spectrum. This is illustrated in Fig. 6.1.

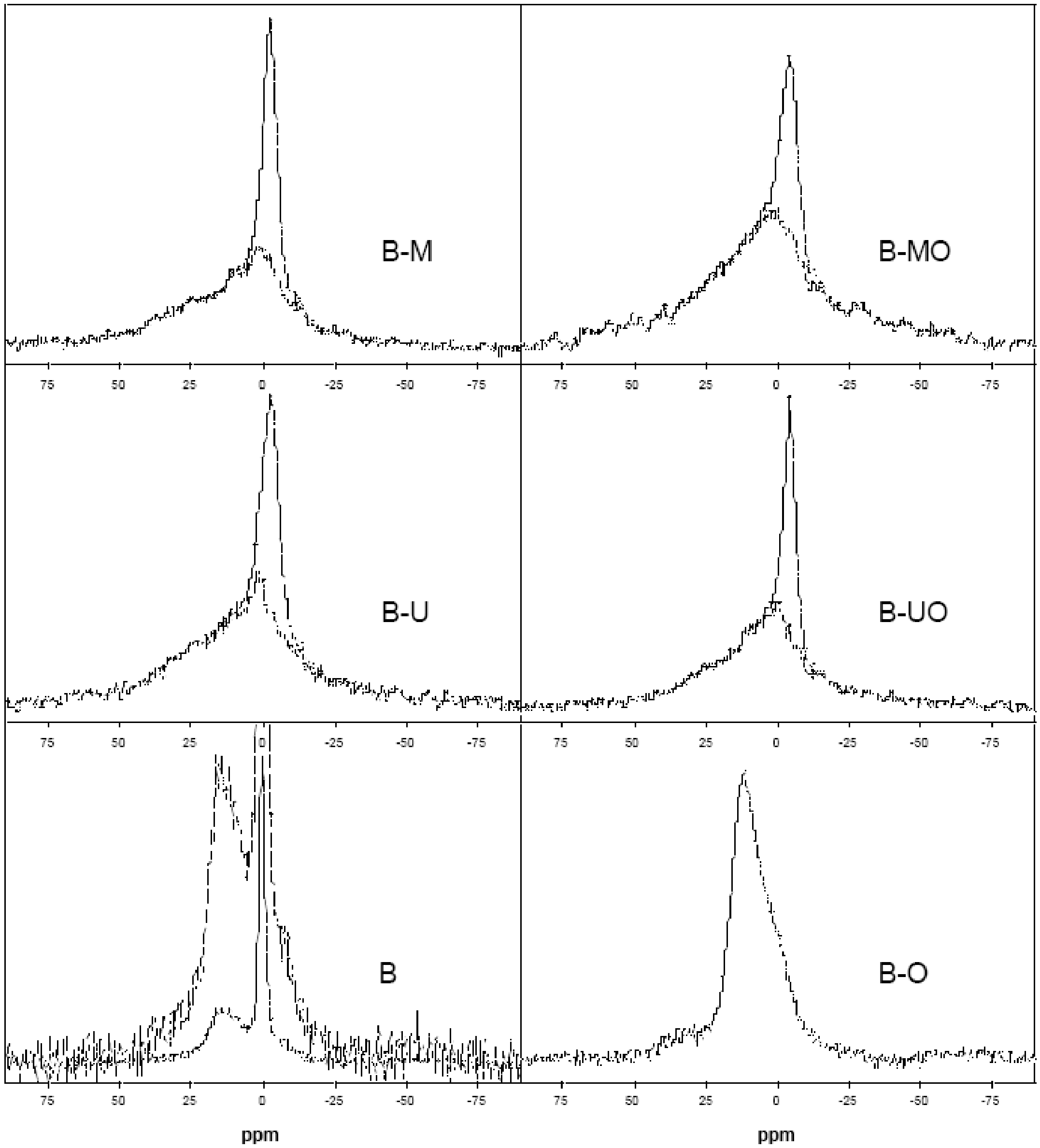

Fig. 6.1 – ^{31}P MAS NMR spectra for carbon samples under the study. The broad component in the spectrum of sample B is also magnified in order to show similarities with that of sample B–O. The broad components are shown for modified samples (B–U, B–UO, B–M and B–MO) by the extended dashed lines under the narrow features.

Cog values and weightings were obtained for each component (Table 1). In the case of narrow component, the cogs are precisely isotropic chemical shifts and their error is small at about ±0.05 ppm. For the broad components, cogs are the average positions of phosphorus sites of large heterogeneity, and the error in these values can be as large as ±2 ppm. Weightings are integrated intensities of the normalized spectra and simply are the fraction of all phosphorus environments associated with each component. The spectral linewidth or full-width at half-maximum (FWHM) is a measure of the phosphorus site distribution within each feature.

Sample	Narrow Component*			Broad Component**		
	cog(ppm)	weight	FWHM(ppm)	cog(ppm)	weight	FWHM(ppm)
B	0.43	0.35	2.1	14.5	0.33	13
	(–1.33	0.02	1.4)	1.2	0.30	25
B-O	– – –	– – –	– – –	11.8	0.70	11
				1.2	0.30	11
B-U	–2.70	0.25	6.3	6.0	0.75	25
B-UO	–4.30	0.24	4.4	4.6	0.76	25
B-M	–2.47	0.27	5.2	6.3	0.73	27
B-MO	–4.20	0.19	6.5	4.3	0.81	33

Table 6.1: Results on ^{31}P MAS NMR analysis [5].

Integrations of the ^{31}P spectra show that about 20–35% of all phosphorus atoms are represented by the narrow component (except for sample B–O). The narrow component cogs falls in the range reported for tetrahedral phosphate environments (PO_4 [3]). The shifts empirically depend on the number of covalent bonds in the tetrahedron and the degree of p-bond character. Pyrophosphate species contain1 bridging oxygen atom and are characterized by isotropic shifts within the range of about 0 to +10 ppm. Some typical pyrophosphates include: $PO_3O_{1/2}^{2-}$, $HPO_3O_{1/2}^{-}$, $H_2PO_3O_{1/2}$. Metaphosphates have 2 bridging oxygens and are more shielded, generally occurring within the range of -20 – 0 ppm. Some examples of metaphosphate species include: $PO_2O_{2/2}^{-}$, $HPO_2O_{2/2}$, *n*-member chain species $P_nO_{3n-1}O_{2/2}^{n-}$, and their protonated analogs.

	Elemental Analysis [%]					XPS			
Sample	C	H	N	O+P/P	N/C	C	O	N	P
B	73.8	3.6	0.2	22.4/0.58	0.003	91.4	6.7	--	0.7
B-O	68.2	2.1	2.0	27.9/0.17	0.03	82.2	15.5	2.2	0.1
B-U	82.2	0.7	5.1	12.0/0.67	0.06	90.0	5.1	3.1	0.6
B-UO	81.4	0.8	5.9	11.9/0.43	0.07	89.7	5.5	3.8	0.4
B-M	83.3	0.6	5.9	10.2/0.60	0.07	89.6	4.0	4.8	0.4
B-MO	79.6	0.9	8.0	11.5/0.41	0.10	86.5	6.8	5.7	0.5

Table 6.2. Carbon, hydrogen, nitrogen, phosphorus and oxygen contents in the samples studied

Resonances from fully covalent phosphate species containing three bridging oxygen atoms, $POO_{3/2}$, are correspondingly shielded (perhaps as much as -40 ppm). The degrees of shielding (more negative shift) and deshielding (more positive shift) are strongly dependent on the P–O bond lengths and P–O–C (and P–O–P) bond angles. The distributions in bond lengths and angles are reflected in the FWHM. As a rough measure, FWHM values generally indicate more structural disorder amongst phosphorus environments upon modification.

Considering the B and B–O samples, the most obvious spectral difference is the absence of a narrow component for the latter. This is purely an oxidation effect and can be correlated with the dramatic reduction of surface phosphorus atoms, as shown by the XPS P data in Table 6.2. It is apparent that surface pyrophosphates present in sample B (at 0.43 ppm) are lost and/or converted into other subsurface phosphorus species as represented within the 11.8 ppm broad component of sample B–O. A minor peak is also found for sample B at -1.33 ppm. This contribution, which could be from surface metaphosphates is also lost or converted upon oxidation.

The similarity between the broad feature of sample B and the entire spectrum of sample B–O (Fig. 6.1) should be noted. Simulation reveals two main subcomponents here: a highly deshielded component and a broad constant component centered at 1.2 ppm. The cog of the deshielded component, being affected by oxidation, reduces from 14.5 ppm to 11.8 ppm and the weighting increases, due to the contribution from converted species. However, the fact that the cogs are so much more deshielded, relative to shifts of typical pyrophosphates, indicates a fundamentally different structure for these phosphorus environments. A substantial presence of P–C and P–N bonds is likely, since molecules containing these bonds typically exhibit large and positive ^{31}P shifts [4]. The constant component cog and weight, as described, is little affected by oxidation. On the other hand, for the B–O sample the FWHM anomalously decreases from 25 ppm to 11 ppm, which might be related to more homogenous surface phosphorus chemistry formed upon strong oxidation and the decrease in relative number of phosphorus atoms on the surface as a result of a significant increase in the oxygen atoms incorporated to the carbon matrix.

With the urea/melamine modification, the narrow component appears broader and more shielded. The presence of the peak is somewhat of a surprise for the preoxidized samples since the narrow component disappears altogether in the B–O sample. As observed with the XPS P data, upon modificationof B–O to form B–UO and B–MO, there is a regeneration of surface phosphates. This phenomenon may occur as a byproduct of the high temperature processing used during the modification and decomposition of a significant number of oxygen containing functional groups. Cogs differ from those for the B and B–O samples by as much as -5 ppm for the narrow component, and -8 ppm for the broad component. In that oxygen depletion where carbon and nitrogen incorporation accompany modification, it is reasonable to assume an enhancement in both P–C and P–N bond formation. However, as mentioned above, these bonds generally yield positive ^{31}P shifts. A more plausible explanation is that upon the modification non-bridging oxygen atoms are converted into covalent bridging oxygen atoms, $P–O^{-} \rightarrow P–O–$, as in the conversion of pyrophosphate into metaphosphate species (i.e. B to B-U: $PO_3O_{1/2}^{2-} \rightarrow PO_2O_{2/2}^{-}$). In this way, the cog of the narrow line reflects an increasing metaphosphate character within the distribution of surface phosphates. The more pronounced negative shift for the preoxidized samples is probably due to the absence of pyrophosphates in the B–O sample. Again, as with the B and B–O samples, there is a fair correlation between the surface phosphorus content, as given by the XPS (X-ray photoelectron spectroscopy) results collected by CITY College's group in Table 6.2 and the relative weight of the narrow components.

Larger cogs are observed for B and B–O; however, the most substantial differences between them and the modified materials are with lineshapes. In that the narrow component has been identified with surface phosphates, the broad component is primarily identified with very heterogeneous subsurface phosphorus environments including phosphates and more complex structures containing multiple P–C, P–N (and P=N) bonds. These distributions are very much different between the nitrogen-containing and the initial materials. Generally, the most deshielded resonances occur with environments containing P–C bonds (around 10 ppm or more) followed by P–N bonds (around 1 ppm or more). The B and B–O samples, display a large proportion of P–C influenced environments as implied by cogs near and above 12 ppm. The most shielded resonances are found for covalent phosphates such as $PO(OP)_3$ and $PO(OC)_3$. Between the deshielded and shielded extremes occur alkyl phosphates (phosphocarbonaceous esters) containing one or two non-bridging oxygens, pyro- and meta-phosphates. The broad component gathered for the modified samples has very large distributions covering the entire range of tetrahedral phosphorus environments; however, the fairly large cogs around 5ppm imply a substantial representation of alkyl phosphates and nitrided phosphorus environments. Finally, it is important to note that for the nitrogen-containing samples, cogs for both broad and narrow components reduce by about 2 ppm with preoxidation. This common difference suggests that the widespread purging of surface pyrophosphate species by oxidation prior to the high temperature modification influences the distribution of surface phosphates (regenerated by modification) as well as the distribution of subsurface phosphorus environments.

Taking into account the above discussion on linking the cog to the chemical environment of phosphorus and the FWHM to the distribution of species, the linear trends between the FWHM of the broad component of the ^{31}P NMR spectra (BFWHM) and the contents of nitrogen and oxygen in our samples indicate their direct contribution to the phosphorous surface compounds (Fig. 6.2). Similar trends were founds for the narrow components FWHM (NFWHM). It is interesting that with an increase in the content of nitrogen as a result of surface modifications new types species are formed, likely those involving P-N and P-C. Since this increase in nitrogen is accompanied by a decrease in the oxygen content and more or less constant phosphorus, it is likely that less oxygen is involved in covalent bonds with phosphorus.

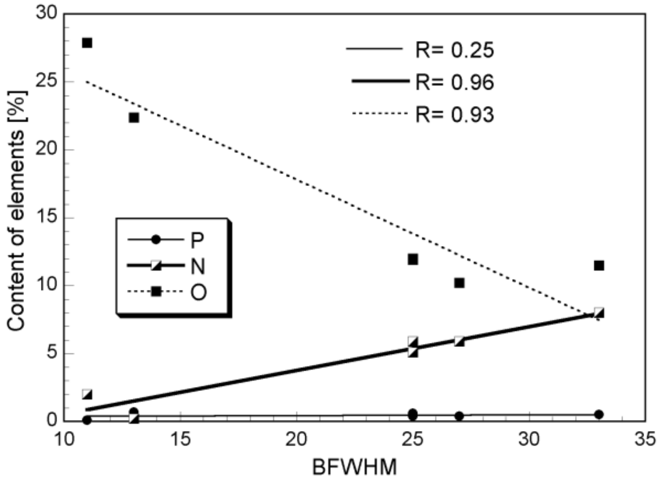

Figure 6.2. Relationship between the content of heteroatoms in carbons and FWHM of the broad components of the ^{31}P MAS NMR spectra [5].

In order to study the effect of phosphorus on capacitance, specific capacitance of modified samples is plotted against the cogs of both the narrow (Ncog) and the broad

(Bcog) components and the corresponding correlations are shown in Figure 6.3. It is observed that deshielding of Ncog and Bcog has positive effect on capacitance and the slope of the lines representing the linear trend for Ncog and Bcog are very similar. As discussed above, the most shielded Ncogs correspond to the surface metaphosphates and from the data shown in Table 6.2 it is evident that the preoxidized samples contain more of these species than their non-preoxidized counterparts. The specific capacitances of B-UO and B-MO are however lower than those of B-U and B-M whose surfaces consist of more pyrophosphates than metaphosphates. This suggests that the surface pyrophosphates have positive effect on the capacitance through some possible Faradaic interactions. Similarity between the slopes of Ncog and Bcog implies the equivalent importance of surface and subsurface phosphorus environment on the capacitive performance of the carbons under the study. In other words, surface phosphates and subsurface structures involving P-N and P=N bondings are confirmed to positively affect the capacitive performance of carbons.

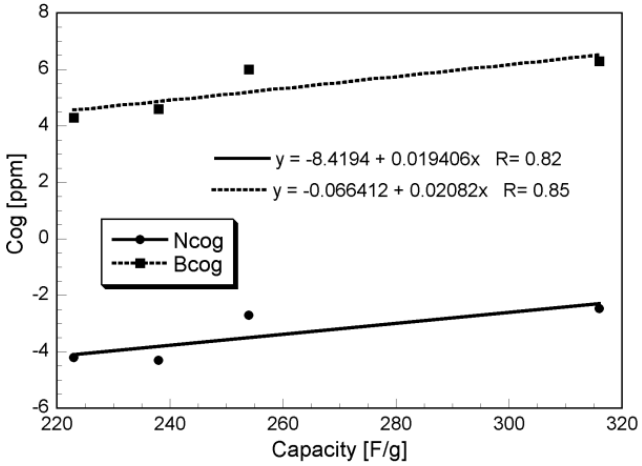

Figure 6.3. Relationship between Cogs of both components of the ^{31}P MAS NMR spectra for the carbons modified with nitrogen and the electrochemical capacitance [5].

Another important aspect is to look at the effect of phosphorus on the capacitance retention at higher current loads. Figure 6.4 displays the relationship between the capacitance retention ratio of modified samples (including the B sample) and the NFWHM and BFWHM. It is evident that the surface P environment represented by NFWHM has more pronounced positive effect than the subsurface phosphorus site distribution reflected in BFWHM. A close look on the weights of the corresponding phosphorus species (Table 6.3) reveals that samples with dominant pyrophosphates retain less capacitance than those consisted of predominant metaphosphates. This trend is opposite to that of the role of surface phosphates on specific capacitance discussed above. The largest specific capacitance of B-M with the most deshielded Ncog (-2.47 ppm) among the treated samples corresponding to pyrophosphates can be explained on the basis of these conclusions. In addition, the lowest capacitance retention of B-M at the current load of 1 A/g is in good agreement with its highest fraction of pyrophosphates reflected in largest weight (0.27) among the treated samples.

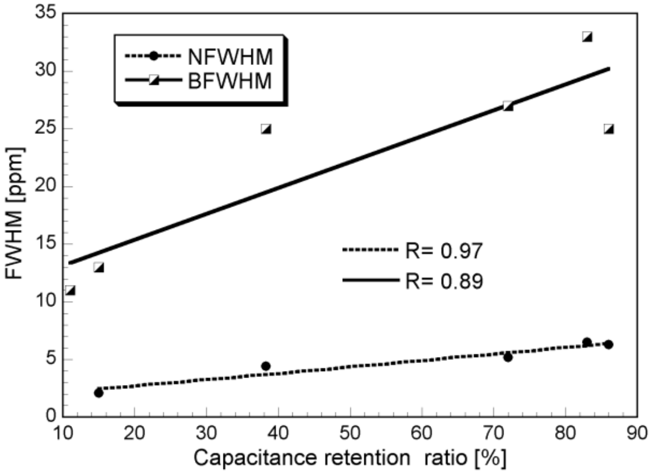

Figure 6.4: Relationship between FWHM of both components of the ^{31}P MAS NMR spectra and the capacitance retention ratio [5].

Sample	Cg at 100 mA/g [F/g]	R_{Cg} [%]
B	208	15
B-O	105	11
B-U	254	86
B-UO	238	86
B-M	316	72
B-MO	223	83

Table 6.3: Electrochemical capacitance, C_g, and capacitance retention ratio R_{Cg} [5].

In the light of these observations, it is anticipated that activated carbons with a higher content of phosphorus will exhibit more significantly enhanced capacitive performance in acidic electrolyte. In addition, this initial study confirmed that both the specific capacitance and capacitance retentions can be controlled by controlling the phosphorus environment.

6.4. **Summary**

The results indicate that upon the incorporation of nitrogen at high temperatures not only new species involving carbon/nitrogen/oxygen are formed but also the phosphorous environment is significantly altered. Both urea and melamine precursors have similar effects on formation of P–N and P–C bonds. These compounds, although present in small but measurable quantities seem to affect the performance of carbons in electrochemical capacitors. With an increase in the heterogeneity of phosphorus containing species and with a decrease in the content of pyrophosphates the capacitance increases and the retention ratio of the capacitor is improved.

References

[1]. Puziy, A.M.; Poddubnaya, O.I.; Martínez-Alonso, A.; Suárez-García, F.; Tascón, J.M.D. "Synthetic carbons activated with phosphoric acid: I. Surface chemistry and ion binding properties" *Carbon* 2002;40:1493-1505.

[2]. Jagtoyen, M.; Derbyshire, F. "Activated carbons from yellow poplar and white oak by H_3PO_4 activation" *Carbon* 1998;36:1085-97.

[3]. Duncan, T.M.; Douglas, D.C. "On The 31P chemical shift anisotropy in condensed phosphates" *Chem. Phys.* 1984;87:339-49.

[4]. Gorenstein D.G. "Phosphorus-31 NMR principles and applications" *New York: Academic Press, Inc*; 1984.

[5].Jurcakova, D.H.; Seredych, M.; Lu, G.Q.; Kodiweera, N.K.A.C.; Stallworth, P.E.; Greenbaum, S.; Bandosz, T.G. "Effect of surface phosphorous functionalities of activated carbon containing oxygen and nitrogen on electrochemical capacitance" *Carbon* 47 (2009) 1576 – 1584.

Bibliography

1. Abragam, A. “Principles of Nuclear Magnetism” *Oxford University Press* 1961.
2. Angewandte, *Chemie International Edition* 41, (2002).
3. Beer, L.; Olmeijer, D.L.; Lefebvre, M.C. “Simultaneous measurement of proton conductivity and methanol permeability for the development of Direct Methanol Fuel Cell Membranes” *PolyFuell Inc, Califonia*.
4. Bouchet, R. *E. Siebert, Solid State Ionics* 118 (1999) 287.
5. Bouchet, R.; Siebert, E. *Solid State Ionics*, **1999**, 118, 287.
6. Burke, A. “Ultracapacitors: why, how, and where is the technology.” *J. Power Sources*, 91 (2000): 37 - 50
7. Callaghan, P.T. “Principles of Nuclear magnetic resonance*” Oxford* (1991).
8. Chandra, S, *Proceedings of the II International Symposium on Solid State Devices*,
9. Choi, J.; Kim, H.D.; Kim, K.H.; Shin, C.; Kim, C.S. “Polymer blend membranes of sulfonated poly(arylene ether ketone) for direct methanol fuel cell.” *Journal of membrane science* 310 (2008): 384 – 392.
10. Choi, J.; Kim, T.; Kim, S.C.; “Nafion-Sulfonated Poly(arylene ether sulfone) Composit Membrane for Direct Methanol Fuel Cell*” Macromolecular Research*. 13 (2005): 514-520
11. Chowdari, B.V.; Radakrishna, S.; Editors. World Scientific Publication, Singapore, **1988**.
12. Chuang, S.H.; Bajue, S.; Greenbaum, S.G. *J. Chem. Phys*. 112 (2000) 8515.
13. Chung, T.S. *J. Macromol. Sci*. **1997**, C37, 277.
14. Crutchfield, M.M; Callis, C.F.; Irani, R.R.; Roth, G.C.; *Inorg. Chem*., **1962**, 1, 813.

15. Dippel, T.; Kreuer, K.D.; Lassegues, J.C.; Rodriguez, D. *Solid State Ionics*, **1993**.
16. Duer, M.J. “Introduction to Solid State NMR Spectroscopy” *Blackwell Publishing* (2004).
17. Duer, M.J. “Solid State NMR Spectroscopy-principles and applications” *Blackwell Science LTD* (2002).
18. Duncan, T.M.; Douglas, D.C. “On The 31P chemical shift anisotropy in condensed phosphates” *Chem. Phys.* 1984;87:339-49.
19. Eco Chemie B.V. “Supercapacitors: Principles and characterization using Autolab”, www.autolab-instruments.com
20. Every, H.A.; Hicker, M.A.; McGrath, J.E.; Zawodzinski Jr, T.A. “An NMR study of methanol diffusion in polymer electrolyte fuel cell membranes” *Journal of Membrane Science* 250(2005) 183-188.
21. Fontanella, J.J.; Wintersgill, M.C.; Wainright, J.C.; Savinell, R.C.; Litt, M. *Electrochim. Acta*. 43 (1998) 1289.
22. Fontanella, J.J.; Wintersgill, M.C.; Wainright, J.S.; Savinell, R.F.; Litt, M. *Electrochim. Acta*, **1998**, 43, 1289.
23. Fukushima, E.; Roeder, S.B.W. “Experimental pulse NMR” *Addison-Wesley Publishing Company,Inc*. (1996).
24. Fulcher, G.S. *J. Am. Ceram*. Soc. 8 (1925) 339.
25. Glipa, X.; Bonnet, B.; Mula, B.; Jones, D.J.; Roziere, J.; Mater. *J.Chem*. 9 (1999) 3045.
26. Gorenstein D.G. “Phosphorus-31 NMR principles and applications” *New York: Academic Press, Inc*; 1984.

27. Hahn, E.L. “Spin Echoes” *Phys.rev*, vol 80(1950).

28. Hickner, M.A.; Fujimoto, C.H.; Cornelius, C.J. “Transport in sulfonated poly(phenylene)s: Proton conductivity, permeability, and the state of water” *Polymer* 47 (2006) 4238–4244.

29. Hore, P.J. “ Nuclear Magnetic Resonance” *Oxford* (2002).

30. Hore, P.J.; Jones, J.A.; Wimperis, S. “NMR: The Tookit” *Oxford* (2002).

31. Jagtoyen, M.; Derbyshire, F. “Activated carbons from yellow poplar and white oak by H_3PO_4 activation” *Carbon* 1998;36:1085-97.

32. Jayakody, J.R.P. *et al., J. Electrochem. Soc*. 154 (2007) B242.

33. Jayakody, J.R.P.; Khalfan, A.; Mananga, E.S.; Greenbaum, G.S.; Dang, T.D.; Mantz, R. “NMR investigation of water and methanol transport in sulfonated polyareylenethioethersulfones for fuel cell applications” *Journal of Power Sources* 156 (2006):195-199.

34. Jayakody,J.R.P.; Chung, S.H.; Durantino, L.; Zhang, H.; Xiao, L.; Benicewicz, Jiang, R.; Kunz, H.R.; Fenton, J.M.; “Sulfonated Poly (Ether Ether Ketone) based membranes for direct methanol fuel cells (DMFC) applications” *the Electrochemical Co Inc*, Abs, 1024, 204th meeting, 2003.

35. Jurcakova, D.H.; Seredych, M.; Lu, G.Q.; Kodiweera, N.K.A.C.; Stallworth, P.E.; Greenbaum, S.; Bandosz, T.G. “Effect of surface phosphorous functionalities of activated carbon containing oxygen and nitrogen on electrochemical capacitance” *Carbon* 47 (2009) 1576 – 1584.

36. Kawahara, M.; Morita, J.; Rikukawa, M.; Sanui, K.; Ogata, N. *Electrochim. Acta* 45 (2002) 1395.

37. Kongstein, D.E.; Berning, T.; Borresen, B.; Seland, F.; Tunold, R. *Energy*, **2007**, 32, 418.

Laboratory, New Mexico.

38. Lassegues, J.C. Mixed Inorganic-Organic systems: *the acid/polymer blends. In: Colomban Ph, editor. Proton conductors, solids, membranes and gels-materials and devices.* Cambridge Univ. Press, **1992**, p. 311.

39. Levitt, M.H. "Spin Dynamics*" John Wiley & Sons, LTD* (2005).

40. Li, Q.; He, R.; Jensen, J.O.; Bjerrum, N. *Chemistry of Mater*. **2003**, 15(26), 4896.

41. Li, Q.; He, R.; Jensen, J.O.; Savinell, R.; Bjerrum, N. *Progress in Polymer Sci*. **2009**, 34, 449.

42. Li, Q.; Hjuler, H.A.; Bjerrum, N.J.; *J. Appl. Electrochem*. 31 (2001) 773.

43. Mehrer, H. " Diffusion in Solids: Fundamentals, Method, Materials, Difusion – Controlled Processes" *Springer*, 2007.

44. Meiboom, S.; Gill, D. " Modified Spin-Echo Method for Measuring RelaxationTimes*"*

The review of scientific instruments, vol 29 (1958).

45. Nicotera, I.; Khalfan, A.; Goenaga, G.; Zhang, T.; Bocarshy, A.; Greenbaum, S. "NMR investigation of water and methanol mobility in nanocomposite fuel cell membranes" *Ionics* 14 (2008):243-253.

46. Othman, M.H.D.; Ismail, A.F.; Mustafa, A.; " Physico-chemical study of sulfonated Poly

(ether ether ketone) membranes for Direct Methanol Fuel Cell applications" *Malaysian*

polymer journal (MPJ), vol 2 (2007): 10 -28.

47. Pavia, D.L.; Lampman, G.M.; kriz, G.S. “Introduction to spectroscopy” *Thomson Learning Inc*, third edition (2001).
48. Puziy, A.M.; Poddubnaya, O.I.; Martínez-Alonso, A.; Suárez-García, F.; Tascón, J.M.D. “Synthetic carbons activated with phosphoric acid: I. Surface chemistry and ion binding properties” *Carbon* 2002;40:1493-1505.
49. Ramsey, N.F. “Magnetic Shielding of Nuclei in Molecules” *Phys.rev*, vol 78(1950).
50. Ravikumar, M.K.; Shukla, A.K. “Effect of methanol crossover in a liquid-feed polymer-electrolyte direct methanol fuel cell” *J. Electrochem. Soc.* 143 (1996).
51. Rayment, C.; Sherwin, S.; “ Introduction to Fuel Cell Technology” *University*
52. Samms, S.M.; Wasmu, S.; Savinell, R.F. *J. Electrochem. Soc*. 143 (1996)1225.
53. Santiago, E.I.; Isidoro, R.A.; Dresch, M.A.; Matos, B.R.; Linardi, M.; Fonseca, F.C. *Electrochim. Acta*. **2009**, 54, 4111.
54. Sarangapani, S.; Lessner, P.M.; LaConti, A.B.; *U.S. Patent 5 136 474* (1992).
55. Sarangapani, S.; Tilak, B.V.; Chen, C.P. *J. Electrochem. Soc.*, 143 (1996).
56. Scott, K.; Taama, W.M.; Argyropoulos, P.; Sundmacher, K.; “The impact of mass
57. Scott, K.; Taama, W.M.; Argyropoulos, P.; Sundmacher, K. “The impact of mass transport and methanol crossover on the direct methanol fuel cell” *J. Power Sources* 83 (1999) 204.
58. Slichter, C.P. “Principle of magnetic resonance” *Happer and Row publishers* (1963).

59. Stejskal, E.O.; Tanner, J.E. “Spin Diffusion Measurements: Spin echoes in the presence of a time- dependant field gradient” *J.Chem.Phys*, vol 42(1964).
60. Tamman, G.; Hesse, W.; Aborg. Z. *Allg. Chem*. 156 (1926) 245.
61. Tanner, J.E. “ Use of the stimulated echo in NMR diffusion studies” *J.chem.phys*, vol 52 (1969).
62. Thomas, S.; Zalbowitz, M.; “ Fuel Cells – green power*”*, *Los Alamos National* transport and methanol crossover on the direct methanol fuel cell” *J. Power Sources*
63. Trassatti, S.; Kurzweil, P.; *Platinum Metals Rev.*, 38 (1994):46-56.
64. Ueki, T.; Watanabe, M. “Macromolecules in ionic liquids: Progress, Challeneges and Oppertunities*” Macromolecules, The American Chemical Society* (2008).
65. Vogel, H. *Phys. Z.* 22 (1921) 645.
66. Wainright, J.S.; Wang, J.; Weng, D.; Savinell, R.F.; Litt, M. J. *Electrochem.Soc*. 142 (1995) L121.
67. Wang, J.T.; Savinell, R.F.; Wainright, J.; Litt, M.; Yu, H. *Electrochim. Acta* 41 (1996) 193.
68. Wang, J.T.; Wainright, J.; Savinell, R.F.; Litt, M. *J. Appl. Electrochem*. 26 (1996) 751.
69. Weng, D.; Wainright, J.S.; Landau, D.; Savinell, R.F. *J. Electrochem. Soc*.143 (1996) 1260.
70. www.occc.edu/kmbailey/Chem1115Tutorials/Molarity.htm, Calculating Molarity.
71. Xiao, L.; Zhang, H.; Scanlon, E.; Ramanathan, L.S.; Chloe, E-W.; Rogers, D.; Apple, T.; Benicewicz, B.C. *Chem. Mater*. **2005**, 17, 5328.
72. Xing, B.; Savadogo, O. *J. New Mater. Electrochem. Systems*, **1999**, 2, 95.

73. Xing, B.; Savadogo, O.*;* *J. New Mater. Electrochem. Syst*. 2 (1999) 95.
74. Ye, H.; Huang, J.; Xu, J.J.; Kodiweera, N.K.A.C.; Jayakody, J.R.P.; Greenbaum, S.G. "New membranes based on ionic liquids for PEM fuel cells at elevated temperature*" Journal of Power Sources* 178 (2008):651–660.
75. Ye, H.; Huang, J.; Xu, J.J.; Kodiweera, N.K.A.C.; Jayakody, J.R.P.; Greenbaum, S.G. j*ournal of power sources* 178 (2008) 651-660.
76. Zheng, J.P.; Jow, T.R.; J. *Electrochem. Soc.*, 142 (1995).
77. Zhu, J. G. 'Super Capacitors' University of Technology, Sydney.